Deciphering the driving forces of erosion rates on millennial to million-year timescales in glacially impacted landscapes: An example from the Western Alps

C. Glotzbach,[1] P. van der Beek,[2] J. Carcaillet,[2] and R. Delunel[3]

Received 20 September 2012; revised 5 July 2013; accepted 9 July 2013; published 16 August 2013.

[1] In many regions, tectonic uplift is the main driver of erosion over million-year (Myr) timescales, but climate changes can markedly affect the link between tectonics and erosion, causing transient variations in erosion rates. Here we study the driving forces of millennial to Myr-scale erosion rates in the French Western Alps, as estimated from *in situ* produced cosmogenic ^{10}Be and a newly developed approach integrating detrital and bedrock apatite fission-track thermochronology. Millennial erosion rates from ^{10}Be analyses vary between ~0.27 and ~1.33 m/kyr, similar to rates measured in adjacent areas of the Alps. Significant positive correlations of millennial erosion rates with geomorphic measures, in particular with the LGM ice thickness, reveal a strong transient morphological and erosional perturbation caused by repeated Quaternary glaciations. The perturbation appears independent of Myr-scale uplift and erosion gradients, with the effect that millennial erosion rates exceed Myr-scale erosion rates only in the internal Alps where the latter are low (<0.4 km/Myr). These areas, moreover, exhibit channels that clearly plot above a general linear positive relation between Myr-scale erosion rates and normalized steepness index. Glacial erosion acts irrespective of rock uplift and thus not only leads to an overall increase in erosion rates but also regulates landscape morphology and erosion rates in regions with considerable spatial gradients in Myr-scale tectonic uplift. Our study demonstrates that climate change, e.g., through occurrence of major glaciations, can markedly perturb landscape morphology and related millennial erosion rate patterns, even in regions where Myr-scale erosion rates are dominantly controlled by tectonics.

Citation: Glotzbach, C., P. van der Beek, J. Carcaillet, and R. Delunel (2013), Deciphering the driving forces of erosion rates on millennial to million-year timescales in glacially impacted landscapes: An example from the Western Alps, *J. Geophys. Res. Earth Surf.*, *118*, 1491–1515, doi:10.1002/jgrf.20107.

1. Introduction

[2] The topographic expression of mountain belts is the result of tectonic processes that create topography and erosion that effectively limits topography [e.g., *Koons*, 1989]. Crustal thickening through convergence leads to isostatically compensated surface uplift, buildup of topography, steepening of river channels and hillslopes, increasing relief, and, as a result, enhanced erosional flux [e.g., *Willett*, 1999; *Montgomery and Brandon*, 2002]. Along with tectonic uplift, rock fracturing induced by deformation increases the likelihood of erosional transport [*Molnar et al.*, 2007]. In addition, potential feedbacks with climate exist; an increase in orographic precipitation, for instance, will increase erosional efficiency and degrade river channels, hillslopes, and relief [e.g., *Whipple et al.*, 1999; *Bonnet and Crave*, 2003]. As a result, millennial to million-year (Myr) scale erosion-rate estimates in fluvially dominated active orogens have been shown to correlate with environmental and morphometric measures such as precipitation rate, local relief, hillslope gradient, hilltop curvature, and channel steepness [e.g., *Gilbert*, 1877; *Summerfield and Hulton*, 1994; *Brandon et al.*, 1998; *Montgomery and Brandon*, 2002; *DiBiase et al.*, 2010; *Hurst et al.*, 2012; *Bermudez et al.*, 2013]. The relation between morphometry and glacial erosion is more complex; however, on the orogen scale, focused erosive efficiency of glaciers around the Equilibrium Line Altitude (ELA), known as the "glacial buzzsaw," is thought to limit the height and thus the relief of mountain belts [e.g., *Brozović et al.*, 1997; *Whipple et al.*, 1999; *Egholm et al.*, 2009]. On the scale of individual catchments, in contrast, valley widening and overdeepening can increase local relief [e.g., *Montgomery*, 2002; *Herman et al.*, 2011; *Valla et al.*,

Additional supporting information may be found in the online version of this article.

[1]Institute of Geology, Leibniz University Hannover, Hannover, Germany.
[2]Institut des Science de la Terre, Université Joseph Fourier, Grenoble, France.
[3]Institute of Geological Sciences, University of Bern, Bern, Switzerland.

Corresponding author: C. Glotzbach, Institute of Geology, Leibniz University Hannover, Callinstr. 30, DE-30167 Hannover, Germany. (glotzbach@geowi.uni-hannover.de)

2169-9003/13/10.1002/jgrf.20107

2011; *Steer et al*., 2012]. Independent of the erosional process, but modulated by tectonic and erosion rates, orogenic systems tend toward a flux steady state, in which the erosional outflux matches the accretional (tectonic) influx [e.g., *Willett and Brandon*, 2002]. When convergence ceases, orogenic topography starts to degrade as the erosional flux is then balanced only partly (≤80%) by isostatic rock uplift.

[3] Feedbacks between tectonics, climate, and erosion have been described in active tectonic settings [e.g., *Beaumont et al*., 1992; *Koons*, 1989; *Whipple and Meade*, 2004; *Willett*, 1999] and may be responsible for rapid exhumation of high-grade metamorphic rocks caused by focused river incision, for instance, in the Himalayan syntaxes [e.g., *Zeitler et al*., 2001], or by orographically enhanced erosion and glaciation, such as at the windwardside of the Southern Alps of New Zealand [e.g., *Koons*, 1990]. Similar but less distinct relations exist in "inactive" orogens such as the Central European Alps. While convergence has ceased in the Central Alps [*Nocquet and Calais*, 2003], Quaternary glaciations appear to have resulted in enhanced erosion and isostatically compensated rock uplift [e.g., *Champagnac et al*., 2007]. Locally, glacial valley incision rates exceeded preglacial rates by up to 1 order of magnitude [*Muttoni et al*., 2003; *Haeuselmann et al*., 2007; *Valla et al*., 2012], leaving behind partly overdeepened trough valleys and associated hanging tributary valleys formed during repeated glaciations. Less is known about the glacial/interglacial variability of erosion rates, but erosion rates are assumed to have decreased since peak erosion rates of 1.1 to 2.9 m/kyr estimated from the postglacial sediment flux of the Alps [e.g., *Hinderer*, 2001; *Van den Berg et al*., 2012]. *Wittmann et al*. [2007] estimated millennial erosion rates of 0.9 ± 0.3 m/kyr in the high crystalline Central Alps using *in situ* produced cosmogenic ^{10}Be measured in stream sediments. These rates, although lower than peak postglacial rates, are approximately twice as high as Myr-scale erosion rates from bedrock thermochronology [e.g., *Vernon et al*., 2008] and correlate positively with recent rock-uplift rates from geodetic measurements. This relation, together with the inference that recent rock-uplift rates amount to about ~80% of the erosion rates, was used to argue that Holocene erosion of the Central Alps is partly balanced by isostatic rock uplift [e.g., *Wittmann et al*., 2007; *Champagnac et al*., 2009].

[4] Recently, several studies have aimed at quantifying the relationships between tectonics, climate, erosion, and resulting basin morphometry using ^{10}Be-derived catchment-wide erosion rates [e.g., *Riebe et al*., 2000; *Matmon et al*., 2003; *Binnie et al*., 2007; *Ouimet et al*., 2009; *DiBiase et al*., 2010, 2012; *Palumbo et al*., 2010; *Henck et al*., 2011]. These studies have confirmed that both soil-mantled and rocky hillslopes are limited by slope stability and thus do not, or only slightly, continue to steepen beyond a threshold gradient/erosion rate [*Schmidt and Montgomery*, 1995; *Montgomery and Brandon*, 2002; *DiBiase et al*., 2012]. Conversely, channels continue to steepen while uplift and erosion rates increase, be it nonlinearly, suggesting that channel steepness is a more reliable geomorphic proxy for rock uplift and erosion rate than hillslope angle or relief. Contrary to these studies in fluvial (nonglaciated) landscapes, ^{10}Be-derived erosion rates appear to be only partly correlated with geomorphic metrics in the Alps [*Wittmann et al*., 2007; *Delunel et al*., 2010; *Norton et al*., 2011]. Only the Central Alps exhibit significant correlations between millennial erosion rates and geomorphic metrics, such as mean elevation, relief, and hillslope [*Wittmann et al*., 2007]; however, these appear to be strongly guided by the inclusion of data from the (low-relief and slowly eroding) foreland. ^{10}Be-derived erosion rates from a single crystalline massif in the Western Alps reveal a positive correlation with elevation in the absence of other correlations, which was used to argue for a climatic control on catchment-wide erosion rates through the temperature (and therefore altitude-) dependence of the efficiency of frost-cracking processes [*Delunel et al*., 2010].

[5] In this study, we investigate the impact of tectonics and climate change on landscape evolution in the Western Alps. Following earlier studies in the Alps [*Wittmann et al*., 2007; *Delunel et al*., 2010; *Norton et al*., 2011], we use *in situ* produced cosmogenic ^{10}Be measurements of stream sediments to quantify millennial erosion rates. In addition, we present a novel approach to extract estimates of millennial-scale lateral variations in erosion rates from detrital thermochronology data. Results of the latter approach are compared with ^{10}Be results, increasing the reliability of inferred spatial variations in erosion rates. Erosion-rate estimates derived from detrital thermochronology and ^{10}Be data are compared to environmental and geomorphic metrics derived from digital elevation model (DEM) analyses as well as to Myr-scale erosion rates from bedrock thermochronology to test the hypothesis that Myr-scale erosion reflects tectonics, and millennial erosion rates are controlled by climate change. Special attention is paid to the glacial impact on landscape morphometry and related potential perturbations of millennial to Myr-scale erosion rates.

[6] The study area encompasses the Belledonne, Vanoise, and Queyras regions of the Western European Alps, immediately north and east of the Ecrins-Pelvoux massif investigated by *Delunel et al*. [2010]. This area is well suited to investigate the relative importance of tectonics and climate in driving erosion rates, because these processes act on different temporal and spatial scales, and our combined analysis allows us to map spatial and temporal variations in erosion rates. At present, there is a weak climate (mean annual precipitation) gradient, but a strong tectonically controlled gradient in Myr-scale uplift and erosion rates in the study area [e.g., *Fügenschuh and Schmid*, 2003; *Tricart et al*., 2006; *Vernon et al*., 2008]; thus, if millennial erosion rates follow the Myr trend, this would argue for a tectonic control. Conversely, millennial erosion rates are perhaps strongly perturbed by extensive Quaternary glaciations, in which case we expected them to be independent of the long-term trend, but instead scale with some climatic or morphometric proxy.

2. Geological and Geomorphic Setting

[7] The study area comprises the Isère drainage basin, upstream of the city of Grenoble, and the Queyras region in the French Western Alps. It consists of different tectono-metamorphic units, belonging to the Helvetic and Penninic domains of the Alps (Figure 1). The Helvetic domain corresponds to the former Eurasian passive margin, whereas the Penninic domain represents the Penninic-Ligurian Ocean basin. During the Alpine orogeny, the Penninic domain has

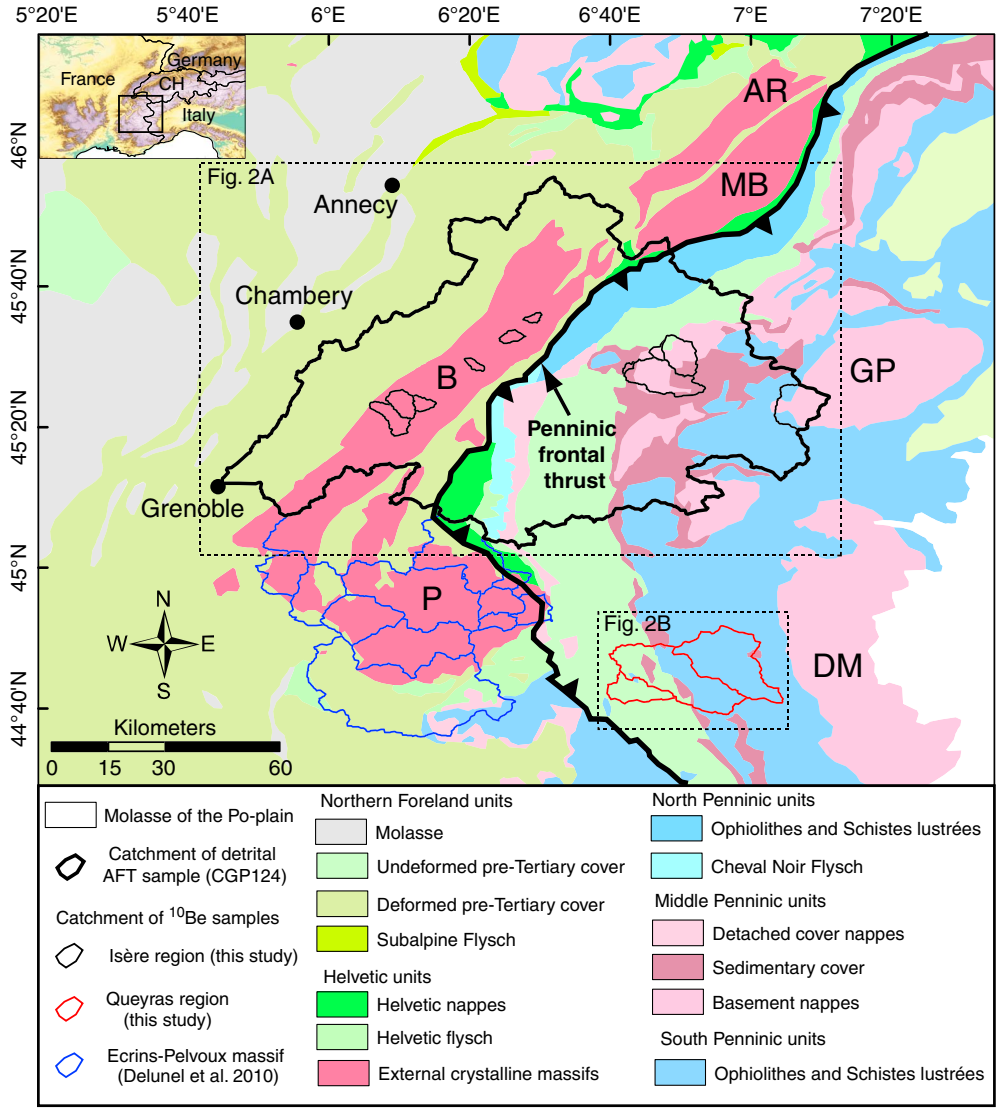

Figure 1. Tectonic map of the central Western Alps [after *Schmid et al*., 2004] with location of analyzed catchments of this study (black and red) and from *Delunel et al*. [2010] (blue). Abbreviations of external and internal crystalline massifs: AR = Aiguilles Rouges, B = Belledonne, DM = Dora Maira, GP = Gran Paradiso, MB = Mont Blanc, and P = Ecrins-Pelvoux.

been thrusted over the Helvetic domain along the Penninic frontal thrust (PFT) [e.g., *Schmid et al*., 2004]. West of the PFT, the study area includes the Belledonne and Ecrins-Pelvoux external crystalline massifs, consisting of Variscan basement and its Mesozoic sedimentary cover. Further east, remnants of the sedimentary infill of the former Penninic-Ligurian Ocean crop out between continental slivers of middle Penninic origin, such as the Gran Paradiso massif (Figure 1).

[8] These once deeply buried units were asynchronously exhumed to near-surface crustal levels, as revealed by thermochronology [e.g., *Seward and Mancktelow*, 1994; *Fügenschuh and Schmid*, 2003; *Malusà et al*., 2005; *Beucher et al*., 2012]. The internal units were exhumed first, as indicated by apatite fission-track (AFT) ages ranging from ~10 to 40 Ma. In contrast, AFT ages of the external massifs and part of the westernmost internal units are <10 Ma, with a minimum age of 1.6 Ma (for a compilation, see *Vernon et al*. [2008]).

[9] At present, the tectonics of the Western Alps is characterized by extension in the core of the orogen and oblique compression in its external parts [e.g., *Sue et al*., 1999, 2007]. In the absence of present-day convergence in the Western Alps [e.g., *Nocquet and Calais*, 2003], it is assumed that buoyancy forces in the core of the orogen balance moderate ongoing compression at its edges [e.g., *Sue et al*., 1999, 2007]. Leveling has revealed present-day rock-uplift rates of up to ~1.5 mm/yr in the Belledonne massif [*Jouanne et al*., 1995]; recent continuous GPS data corroborate these and suggest similarly high rates in the Vanoise region of the internal western Alps [*Brockmann et al*., 2009; *Nocquet et al*., 2011].

[10] The study area was strongly glaciated during the Quaternary, with Last Glacial Maximum (LGM) ice-surface elevations ranging from 1.2 km in the Isère Valley near Grenoble to 2.6 km in the Grand Paradiso massif [e.g., *Kelly et al*., 2004; *Coutterand*, 2010; *Delunel*, 2010]. The

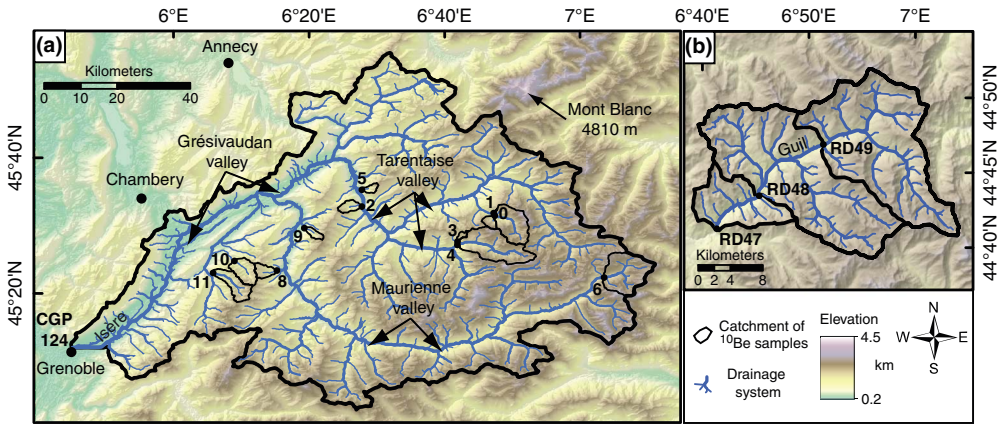

Figure 2. Topographic map of (a) the Isère catchment upstream of Grenoble and (b) the Queyras region, derived from a SRTM DEM with a resolution of 90 m (for location, see Figure 1). Numbers of sample localities in Figure 2a appended to CGP200 give sample code.

ELA of glaciers was at elevations of 1.8 ± 0.1 km during the LGM [*Ivy-Ochs et al*., 2006; *van der Beek and Bourbon*, 2008], approximately 1.1 km lower than the present-day ELA located at ~2.9 km [*Vincent*, 2002; *Rabatel et al*., 2005]. Glacial flow directions approximately followed the present-day drainage network, with major valley glaciers flowing down the Maurienne and Tarentaise Valleys joining the Isère ice stream (for location, see Figure 2). During maximum glaciation, only the highest mountain peaks stood above the ice surface as nunataks. The main valley glaciers rapidly retreated during the Late Glacial stage (15–20 ka BP), followed by several lesser glacier advances [e.g., *Ivy-Ochs et al*., 2008; *Delunel*, 2010]. The most recent, and arguably smallest, advance happened during the seventeenth to nineteenth century Little Ice Age (LIA), but was confined to cirques [e.g., *Ivy-Ochs et al*., 2008]. Today, glaciers in the study area are restricted to high-elevation regions (>2.6 km). The general retreat of glaciers since the LGM has exposed hillslopes that are partly blanketed by loose glacial deposits produced by enhanced LGM and Late Glacial erosion compared to moderate Holocene rates [e.g., *Hinderer*, 2001].

[11] The geomorphological imprint of Quaternary glaciations is profound and includes overdeepened valleys such as the Isère Valley, which was carved to >300 m below sea level and was filled rapidly after deglaciation until 12 ka BP [*Nicoud et al*., 2002], U-shaped valleys, hanging tributaries, high-elevation low-relief rock shoulders, and steep mountain peaks [e.g., *van der Beek and Bourbon*, 2008] (Figures 2 and 3). River long profiles of the upper reaches of the Maurienne and Tarentaise Valleys present a succession of valley steps and flats, typical for glacially influenced river profiles [e.g., *MacGregor et al*., 2000; *Anderson et al*., 2006]. The topographic steps partly correlate with the position of the ELA during the LGM and Late Glacial stages (Figure 4a; for more examples, see Figures S1–S4), and thus are assumed to be the result of efficient glacial erosion around the ELA [e.g., *Brozović et al*., 1997; *Anders et al*., 2010; *Sternai et al*., 2011]. As a consequence, main valley floors were deepened, leading to development of hanging valleys, and corresponding tributary river profiles exhibit negative concavities (Figure 4e; Figures S5–S9). Hypsometries of analyzed catchments often show a maximum between the LGM and present-day ELAs (Figures 4d, 4h, and S12), similar to catchments in the Ecrins-Pelvoux massif [*van der Beek and Bourbon*, 2008, Figure 7].

3. Sampling Strategy

[12] Eleven subcatchments of the Isère drainage basin and three subcatchments of the Guil River, a tributary of the Durance, were sampled for the calculation of ^{10}Be-derived catchment-wide erosion rates (Figures 1 and 2 and Table 1). We sampled sandbars of active stream channels upstream of major confluences (except for sample CGP201) and visually inspected aerial photographs to exclude catchments with clear evidence of large landslides, which potentially impact ^{10}Be-derived erosion rates [e.g., *Niemi et al*., 2005; *Yanites et al*., 2009; *Kober et al*., 2012]. Various erosional processes typical for Alpine settings are active in the study area; within the headwaters of sampled catchments, rock falls, debris flows, and (periglacial) glacial erosion occur, whereas fluvial erosion dominates the lower reaches of the analyzed catchments.

[13] We focused our sampling on lithologically homogeneous catchments with a high fraction of quartz-bearing rocks. For this reason, some of the sampled catchments are relatively small, especially in the Tarentaise Valley. In the internal Alps, especially along the Guil River, sampled catchments are large to ensure sufficient concentration of quartz by erosional/weathering processes and mixing of sparsely quartz-bearing schists and Quaternary deposits (predominantly LGM in age). Major valleys with abundant flats (Figures 2 and 3) are not sampled to guarantee that the residence of sediments is insignificant compared to the time needed to erode one attenuation length [e.g., *von Blanckenburg*, 2005]. The frequency of flat areas (<3°) in analyzed catchments is between 0.1 (CGP203) and 3.1% (CGP206); for most catchments, it is around 1% (Figures 3 and 4; Figure S12). Therefore, we decided to include valley floors in our analysis, although they may not deliver sediments to the present fluvial system. Sampled catchments can be subdivided according to their lithology and glacier cover into three distinct groups: (i) catchments in the Belledonne massif comprise nearly solely crystalline rocks with minor Quaternary cover and glaciers are not present today; (ii) subcatchments of the Isère drainage basin in the Vanoise region are composed of various meta-sedimentary

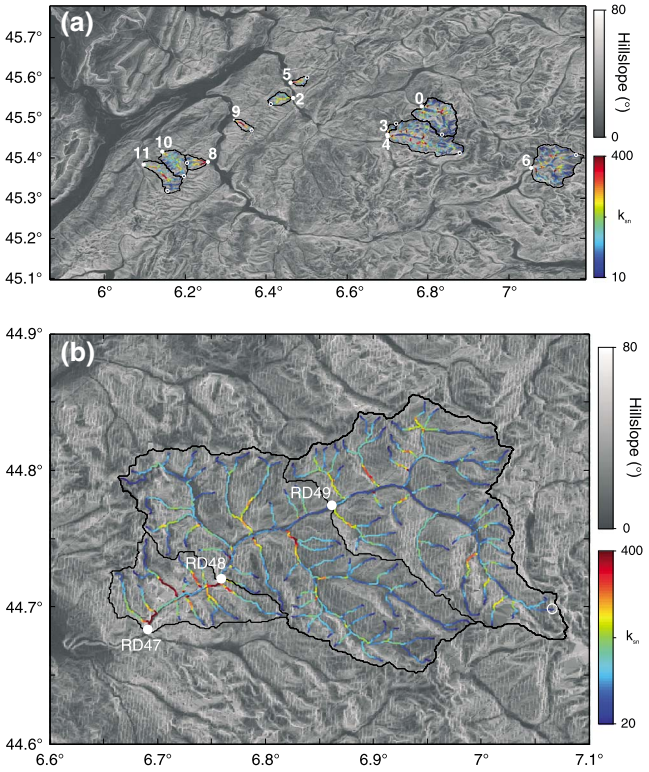

Figure 3. Hillslope map and normalized steepness indices (k_{sn}) of (a) the Isère catchment and (b) the Queyras region, derived from a SRTM DEM with a resolution of 90 m (approximately similar extend as Figure 2). Normalized steepness indices (k_{sn}) are color coded for sampled stream segments with drainage areas >1 km^2. k_{sn} values were calculated with Stream Profiler available at http://www.geomorphtools.org and normalized with a concavity index of 0.45 [e.g., *Ouimet et al*., 2009; *DiBiase et al*., 2010]. White dots mark sample locations, and white circles are the upstream position of river profiles extracted with Stream Profiler and shown in Figure 4 (and Figures S2–S11). Numbers of sample localities in Figure 3a refer to sample code plus CGP200.

rocks and are partly covered by Quaternary deposits and glaciers; and (iii) the Guil catchments in the Queyras region are underlain by different types of schists (mainly Schistes Lustrés) and are generally covered by extensive Quaternary deposits, but lack modern glaciers (Figures 1 and 10).

4. Methods and Analytical Procedure

[14] In this study, we applied *in situ* produced cosmogenic ^{10}Be and AFT thermochronology analyses of stream sediments to estimate absolute and relative rates of surficial mass removal from the Earth's surface by mechanical and chemical processes, which are defined as "erosion" [e.g., *Ring et al*., 1999]. Strictly speaking, thermochronology measures rates of cooling, which can be interpreted as rates of unroofing (exhumation) assuming a transient or steady state geothermal gradient [e.g., *Reiners and Brandon*, 2006; *Willett and Brandon*, 2013]. Exhumation is the integral of tectonic and erosional processes both occur in convergent orogens such as the Alps, for instance, major tectonic unroofing occurred along the long-angle detachment of the Simplon fault zone [e.g., *Campani et al*., 2010]. The absence of such major extensional structure in our study area, however, lets us assume that the dominant exhumational process was erosion.

4.1. Morphometric and Environmental Measures

[15] We performed a detailed geomorphic analysis and extracted a variety of environmental and morphometric measures (such as river long profiles, hillslope, normalized geophysical relief, and steepness index), which are reported in Table 2 and Figures 3 and 4 (also see Figures S1–S12). The geomorphic analysis was performed on a Shuttle Radar Topography Mission (SRTM) DEM with a resolution of 90 m [*U. S. Geological Survey* (*USGS*), 2006]. Reported catchment-averaged geomorphic values are of quartz-bearing grid cells only, but in grid cell-based scatterplots, we also report measures of nonquartz-bearing grid cells. River profiles and mean morphometric measures of sampled catchments are analyzed and compared to millennial and Myr-scale erosion rates to assess the long- and short-term driving forces of landscape evolution.

[16] Studies in steady state fluvial landscapes have shown that geomorphic parameters (in particular the fluvial steepness index) scale with uplift and erosion [e.g., *DiBiase et al*., 2010] and can thus be used to estimate otherwise difficult to measure millennial to Myr-scale uplift rates [e.g., *Lague et al*., 2000; *Cyr et al*., 2010; *Kirby and Whipple*, 2012]. Changes in uplift rate, base-level variations, and glacial erosion will perturb landscapes, and depending on the response time of the system, which mainly depends on the basin size and uplift/erosion rate, a new steady state is

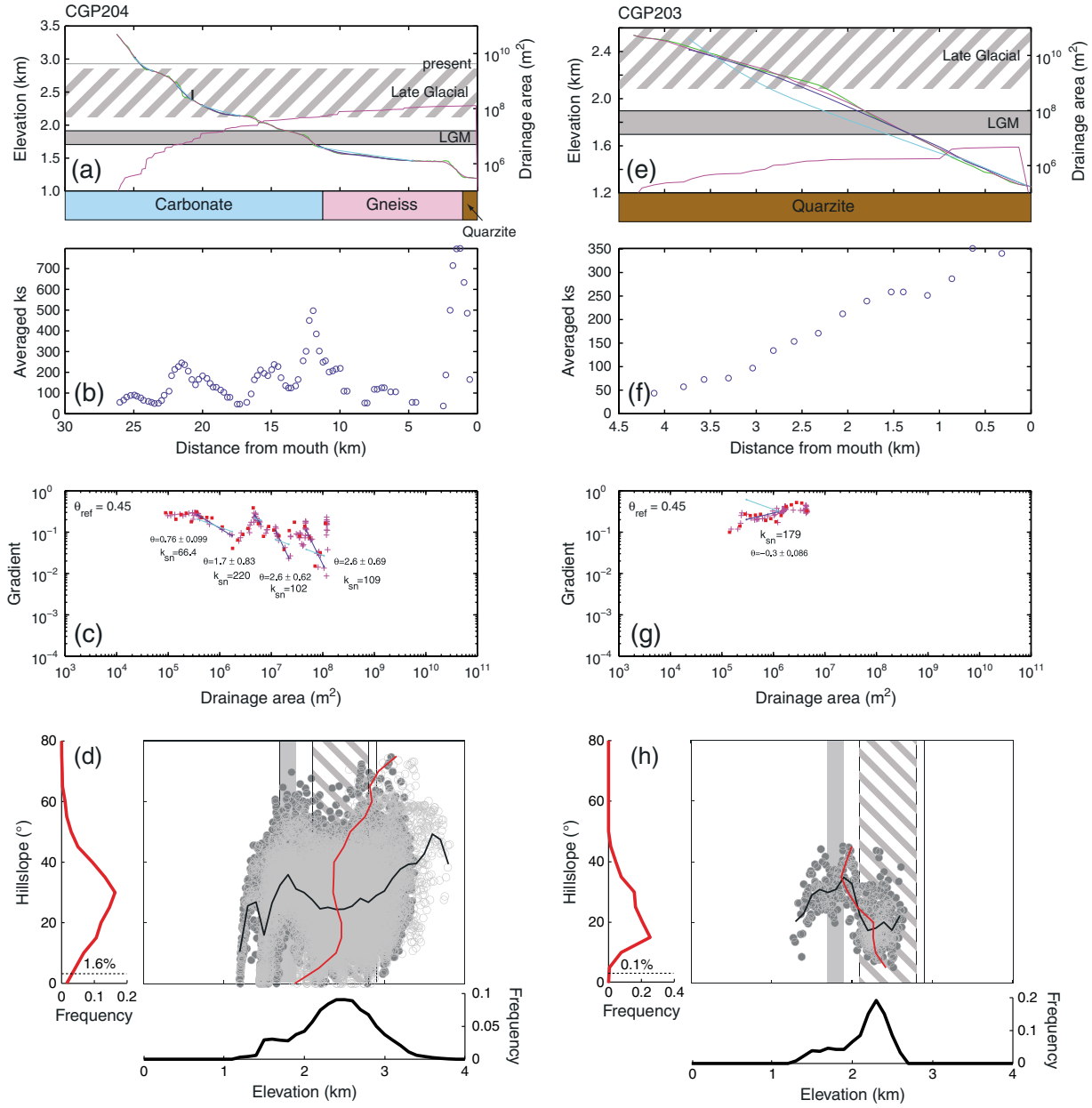

Figure 4. River long profile, drainage area, average k_{sn}, and slope-area plot of the main stream, and hillslope-elevation scatterplot and histograms of catchment CGP204 and CGP203 (for location, see Figures 2 and 3). (a and e) River long profile with lithology (from 1:50000 geological maps) and position of ELA during LGM, Late Glacial, and LIA stages [*Ivy-Ochs et al.*, 2006]. Raw elevations are in green, smoothed in pink and dark blue, and cyan curves are river profile elevations of manually selected river segments predicted by fitted profiles with a reference concavity of 0.45 and best-fit concavity. Black vertical line in Figure 4a marks the terminal elevation of present-day glacier. (b and f) Average k_{sn} values of river profile segments calculated with Stream Profiler (available at http://www.geomorphtools.org) and normalized with a concavity index of 0.45. (c and g) Slope-area plot with manually fitted river segments and resulting concavities and k_{sn} values normalized with a reference concavity of 0.45. (d and h) Elevation-hillslope scatterplot with altitudinal dependence of hillslopes (thin black line) and hillslope dependence of elevations (thin red line). Grey circles are all grid cells, and grey dots are grid cells from quartz-bearing lithologies only. Elevation/hillslope dependence lines are mean values of all grid cells within 100 m and 5° bins, respectively. The vertical grey shaded and hatched areas represent the position of the LGM and Late Glacial ELAs, and the present-day ELA is shown as vertical black line. Corresponding hypsometry and hillslope histograms are shown on the side. Dashed horizontal line marks a hillslope of 3°, and catchment area <3° is given in percent.

Table 1. Sample Locations of Analyzed Stream Sediments

Catchment	Sample Name	Sample Position		
		Latitude	Longitude	Elevation (m)
Torrent le Ponturin	CGP 200	45.52829	6.78551	1487
Torrent le Ponturin	CGP 201	45.52697	6.78726	1504
Torrent du Pussy	CGP 202	45.54870	6.46620	432
Ruisseau le Remous	CGP 203	45.45374	6.69739	1198
Torrent le Doron de Champagny	CGP 204	45.45359	6.70162	1197
Torrent de la Gruvaz	CGP 205	45.58740	6.46035	482
L'Arc	CGP 206	45.37422	7.05711	1823
Ruisseau de la Freche	CGP 208	45.39033	6.25483	527
Ruisseau de la Balme	CGP 209	45.49377	6.32131	511
Torrent le Bens	CGP 210	45.41417	6.14452	788
Torrent le Veyton	CGP 211	45.38345	6.09737	615
Guil	RD47	44.68100	6.69700	1050
Guil	RD48	44.71900	6.76200	1200
Guil	RD49	44.77800	6.86000	1440

typically reached on a million-year timescale [e.g., *Whipple*, 2001; *Whittaker and Boulton*, 2012]. In the study area, due to enhanced erosion capacity of trunk valley glaciers and related valley widening and/or deepening, hanging valleys developed in tributary streams [e.g., *Penck*, 1905; *MacGregor et al*., 2000]. Since deglaciation, hanging valleys have been loci of enhanced erosion [e.g., *Norton et al*., 2008; *Valla et al*., 2010], but due to their long response time, these landscapes are still far out of equilibrium with current climate conditions. Although not in steady state, geomorphic measures combined with erosion estimates can be applied to estimate landscape perturbation and readjustment [e.g.,

Table 2. Mean Environmental/Morphometric Indices of Catchments From the Isère and Queyras regions (This Study) and the Ecrins-Pelvoux Massif [*Delunel et al*., 2010][a]

Sample name	Drainage Area (km^2)	% Quartz Bearing Lithologies	% Quaternary Deposits[b]	% Glacier Extent[c]	LGM Ice Thickness (m)[d]	Elevation (m)	Slope (°)[e]	Relief (m)[f]	k_{sn}[g]	Annual Precipitation (mm/yr)[h]	Long-Term Exhumation (km/Myr)[i]
CGP 200	39	67	21	4	82	2483	29.0	470	147	1495	0.16
CGP 201	32	64	21	4	82	2489	29.0	468	147	1497	0.16
CGP 202	8	66	15	0	328	1596	25.9	168	199	1590	0.65
CGP 203	4	100	28	0	127	2127	23.6	117	207	1183	0.19
CGP 204	60	66	18	25	151	2290	28.7	585	161	1390	0.15
CGP 205	6	100	0	0	273	1592	31.0	143	225	1441	0.70
CGP 206	51	50	18	54	83	2715	22.0	510	140	1276	0.12
CGP 208	11	88	16	0	119	1854	27.8	202	239	1632	0.54
CGP 209	5	74	10	0	217	1745	34.2	263	264	1842	0.72
CGP 210	28	97	12	0	81	1735	27.7	366	156	1497	0.33
CGP 211	29	94	17	0	91	1756	27.9	296	162	1622	0.36
RD47	476	0	50	0	215	2216	24.3	852	145	879	0.16
RD48	421	0	49	0	187	2250	23.8	784	137	882	0.17
RD49	199	0	35	0	133	2305	25.0	596	136	904	0.23
Rd01	613	57	-	-	181	2222	32.8	1037	175	1320	0.46
Rd02	260	86	-	-	110	2413	36.1	798	187	1270	0.49
Rd03	100	47	-	-	177	2616	33.1	672	164	1200	0.55
Rd04	21	91	-	-	140	2510	30.1	331	151	1203	0.30
Rd05	44	92	-	-	78	2765	34.3	533	169	1343	0.48
Rd06	19	72	-	-	60	2674	36.1	373	196	1360	0.53
Rd07	84	75	-	-	118	2603	34.1	623	176	1294	0.38
Rd08	62	82	-	-	45	1741	32.4	645	147	1325	-
Rd09	156	63	-	-	111	1836	34.5	704	166	1253	0.35
Rd10	102	81	-	-	23	1995	35.6	659	175	1310	0.38
Mb130	545	69	-	-	61	1825	27.1	901	131	1259	0.33
Mb146	159	81	-	-	37	1980	34.8	746	188	1385	0.40

[a]Values are averages for areas with quartz-bearing lithologies only.
[b]Surface coverage with Quaternary deposits mapped from 1:50000 scale geological maps.
[c]Surface coverage with present-day glaciers mapped from 1:50000 scale geological maps.
[d]LGM-ice thickness calculated by subtracting the present-day topography from the LGM ice-surface map of *Coutterand* [2010].
[e]Slope, calculated as the arc tangent of the steepest gradient of a 3×3 moving window (eight neighbor cells).
[f]Ridgeline geophysical relief calculated with the approach described in detail by *Brocklehurst and Whipple* [2002].
[g]k_{sn} is the steepness index normalized with a reference concavity of 0.45 calculated with Stream Profiler (http://www.geomorphtools.org).
[h]Annual precipitation rates from measurements between 1971 and 2000 [*Auffray et al*., 2000].
[i]Long-term exhumation rates derived from 1-D steady state thermal modeling of an interpolated surface AFT map (for details see section 4.3).

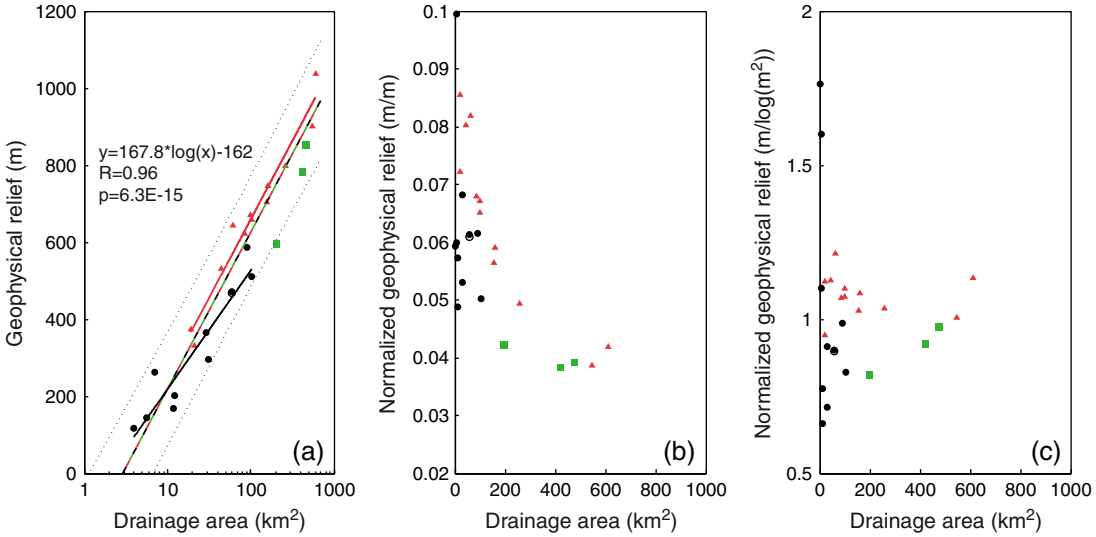

Figure 5. Relation between drainage area and relief. (a) Semi-logarithmic scatterplot of mean ridgeline geophysical relief and drainage area. Black dots, red triangles, and green squares are catchments in the Isère drainage basin, the Ecrins-Pelvoux massif, and the Queyras region, respectively. Best-fit nonlinear regressions are plotted for the whole data set (black-red-green line) with 95% confidence interval, for the Ecrins-Pelvoux data (in red) and the Isère data (in black). Regression function, correlation coefficient, and *p*-value of the significance of the correlation from *t*-statistics are shown in Figure 5a for the whole data set. The corresponding relationship for the Ecrins-Pelvoux (Isère) data subset is: $y = 175.7*\log(x) - 151$ ($y = 133.5*\log(x) - 87.9$), $R = 0.98$ ($R = 0.95$) and $p = 6.8 \times 10^{-9}$ ($p = 5.2 \times 10^{-6}$). (b) Relation between drainage area and mean ridgeline geophysical relief divided by the square root of drainage area. (c) Relation between drainage area and the ratio of the measured and predicted (from the function fitted to the whole data set in Figure 5a) mean ridgeline geophysical relief.

Norton et al., 2010a, 2010b; *Olivetti et al.*, 2012; *Whittaker and Boulton*, 2012].

[17] Hillslope is defined here as the inverse tangent of the steepest gradient of a 3 × 3-moving window (eight neighbor cells), whereas mean hillslope includes flat areas and valley bottoms. For each sampled catchment, we derived elevation-hillslope scatterplots with corresponding elevation histograms (hypsometry), hillslope histograms, altitudinal dependence of hillslopes, and hillslope dependence of elevations. Calculated histograms and dependencies are for all grid cells including quartz-free lithologies. Hypsometries were binned in 100 m intervals, and mean hillslopes were calculated for each interval. Similarly, hillslope histograms were binned in 5° intervals, and mean elevations were calculated for each interval (Figures 4d and 4h).

[18] The relief of landscapes varies with scale and the method by which relief is calculated [e.g., *Brocklehurst and Whipple*, 2002]. We calculated the geophysical relief [*Small and Anderson*, 1998], which is the difference between a surface encompassing all ridgelines and the present-day topography, using the approach described in detail by *Brocklehurst and Whipple* [2002]. Ridgelines of each catchment were isolated and used to interpolate a smooth cubic spline surface. Locations within the catchment that stuck out of the interpolated surface were iteratively added to the ridgeline data, and interpolation of the cubic spline surface was repeated until the interpolated surface overtopped all grid cells of the SRTM DEM. The corresponding geophysical relief can be obtained by subtracting the present-day surface from the interpolated surface and averaged by dividing by catchment area (for example, see Figure S14). Mean basin relief scales logarithmically with basin area (Figure 5a; see also *Brocklehurst and Whipple* [2002, Figure 7]); therefore, we normalized the geophysical relief. Dividing basin-average relief by basin area does not reduce the dependence. Basin-average relief divided by the square root of basin area results in a dimensionless measure of the geophysical relief, which, however, still shows dependence on basin area (Figure 5b). A measure of relief that is independent of basin area, which we call normalized geophysical relief, can be obtained by normalizing with the fitted logarithmic function (Figure 5c).

[19] Commonly, a power law relationship exists between the local slope (S) of fluvial channels and the corresponding drainage area (A), known as Flint's law [*Hack*, 1957; *Flint*, 1974]

$$S = k_s \cdot A^{-\theta} \tag{1}$$

where k_s is the channel steepness index and θ is the concavity index. Regression analysis between S and A can be used to obtain characteristic k_s and θ for selected river channels. However, since k_s and θ are strongly correlated, comparing different channels requires choosing a reference concavity to obtain normalized steepness indices [e.g., *Wobus et al.*, 2006; *Kirby and Whipple*, 2012]. Here we follow recent analyses in fluvial and glacial mountainous landscapes [e.g., *Ouimet et al.*, 2009; *DiBiase et al.*, 2010; *Norton et al.*, 2011], normalizing the steepness index (k_{sn}) to a fixed reference concavity of 0.45 using Matlab® and ArcGIS® scripts available at http://www.geomorphtools.org. Although fitted concavities and associated k_{sn} values can be highly

variable (Figures 4 and S1–S11), a study in the Central and Eastern Alps showed that relative changes in k_{sn} are not significantly affected by applying different reference concavities [*Norton et al*., 2010b].

[20] While fluvial erosion is the dominant erosion process today, large parts of the landscape bear witness to glacial erosion. Quantifying the impact of extensive previous glaciations on Holocene erosion rates is challenging. The efficiency of glacial erosion is assumed to depend primarily on the basal sliding velocity of glaciers [e.g., *Humphrey and Raymond*, 1994; *Hallet et al*., 1996], which is difficult to estimate especially for past glaciations, as it requires application of complex glacier models, knowledge of the preglacial topography, and accounting for the effect of subglacial melt-water and sediment [e.g., *Herman et al*., 2011; *Egholm et al*., 2012]. A snapshot of past basal sliding and thus glacial erosion can be obtained from the product of ice thickness and slope of the ice surface [e.g., *Nye*, 1952]. Rapid headward retreat of glacial erosion [e.g., *Shuster et al*., 2011], however, impedes using this approach to quantify time-integrated glacial erosion. Here we used the mean LGM ice thickness as a proxy for the potential effect of time-integrated glacier erosion [e.g., *Whipple et al*., 1999; *Brocklehurst et al*., 2008], which we calculated by subtracting the present-day topography from the LGM ice-surface map of *Coutterand* [2010]. In addition, the extents of present-day glaciers and widespread glacial deposits were mapped from 1:50000 scale geological maps.

4.2. ^{10}Be-Derived Catchment-Wide Erosion Rates

[21] Cosmic rays interact with target elements in the Earth's atmosphere and surface to produce cosmogenic nuclides, including ^{10}Be (see *Dunai*, [2010] for a review). The production of ^{10}Be decreases exponentially with depth in the uppermost few meters of the Earth's surface; the ^{10}Be nuclide concentration of an eroding surface will reach steady state (i.e., production equals loss induced by radioactive decay and erosion) after continuous removal of several attenuation length-scales. Instead of sampling pointwise locations, a more synoptic view of catchment-wide erosion rates can be obtained from sampling erosional products carried by streams exiting the catchments [e.g., *Brown et al*., 1995; *Riebe et al*., 2000; *von Blanckenburg*, 2005]. In this case, the ^{10}Be concentration C measured in well-mixed stream sediment is related to the mean catchment production rate $\overline{P}$ and erosion rate E following [*Lal*, 1991]

$$C = \frac{\overline{P}}{\lambda + E/\Lambda} \tag{2}$$

in which λ is the ^{10}Be decay constant ($5.00 \pm 0.06 \times 10^{-7}\,\mathrm{yr}^{-1}$) [*Chmeleff et al*., 2010; *Korschinek et al*., 2010], ρ is rock density (e.g., $2.7\,\mathrm{g\,cm}^{-3}$) and Λ is the characteristic attenuation length for ^{10}Be production with depth (~$150\,\mathrm{g\,cm}^{-2}$). From equation (2), a mean time-integrated catchment-wide erosion rate E can be calculated [e.g., *Brown et al*., 1995] assuming that (i) erosion within the catchment is constant over the time needed to denude one attenuation-length scale (erosional timescale), (ii) production rates are corrected for differences in the quartz-content and grain size of contributing lithologies, and (iii) the residence time of sediments within the catchment is insignificant compared to the erosional timescale [e.g., *von Blanckenburg*, 2005]. The major unknown in equation (2) is the mean production rate, which, in this study, has been estimated using available Matlab® functions from the CRONUS-Earth project (http://hess.ess.washington.edu/). At each grid cell of corresponding catchments, the surface production rate P_i, shielding S_i, and relative quartz contribution L_i were estimated, and the mean production rates were calculated [cf. *Delunel et al*., 2010, equation (2)]:

$$\overline{P} = \frac{1}{n}\sum_{i=1}^{n}(P_i \cdot S_i) \tag{3}$$

$$S_i = S_i^t \cdot S_i^g \cdot S_i^s \tag{4}$$

$$n = \sum L_i \tag{5}$$

where n is the number of grid cells that contain quartz-bearing lithologies in the corresponding catchment and S_i^t, S_i^g, and S_i^s are shielding factors of the i-th grid cell due to topography (including self-shielding), glaciers and snow, respectively. A present-day, spallogenic sea-level high-latitude (SLHL) production rate of 4.49 ± 0.39 atoms/g/yr [*Balco et al*., 2008] (see also http://hess.ess.washington.edu) was scaled for altitude and latitude using scaling factors proposed by *Stone* [2000] and assuming spallogenic, stopped and fast muon fractions of the total production equal to 0.9785, 0.015, and 0.0065, respectively. Shielding S^t, including topographic and self-shielding, was estimated for each grid cell of a SRTM DEM with a resolution of 90 m following *Dunne et al*. [1999]. A viewshed function was applied to each grid cell of corresponding catchments to find all surrounding visible grid cells, and from this, the maximum inclination of the horizon in 10° orientation steps was used to calculate the topographic shielding. Note that due to terrain smoothing, calculated shielding factors are maximum estimates and "true" shielding factors may be up to 10% lower [*Norton and Vanacker*, 2009].

[22] We used the present-day glacier extent (mapped from 1:50000 scale geological maps) as a proxy for glacier shielding S^g during the time represented by the erosional timescale. A value of 1 is assigned to S^g for all grid cells, except those covered by present-day glaciers that are set to 0. Note that by assuming zero ^{10}Be production rates below present-day glaciers, we potentially overcorrect the glacial shielding effect on production rates, especially the muogenic production. Measurements of recent glacier outwash material have revealed that the assumption of zero concentration is not always true, as outwash material can contain considerable concentrations of ^{10}Be due to complex exposure histories [*Wittmann et al*., 2007; *Delunel*, 2010]. Only two of our sampled catchments have considerable glacial area (>10%), and thus catchment-wide erosion rates are minimum estimates for these samples.

[23] The combined effects of former (LGM) glacier erosion, shielding, and incorporation of glacial sediments can further bias catchment-wide erosion rates. According to the approach of *Wittmann et al*. [2007], we have investigated whether surface ^{10}Be concentrations (of both bedrock and glacial sediments) have reached steady state after potential zeroing since 15 ka (LGM). 1-D modeling results imply that present-day surface ^{10}Be concentrations have not reached steady state, and thus calculated ^{10}Be-derived erosion rates are overestimated by 3 to 28% for modeled erosion rates

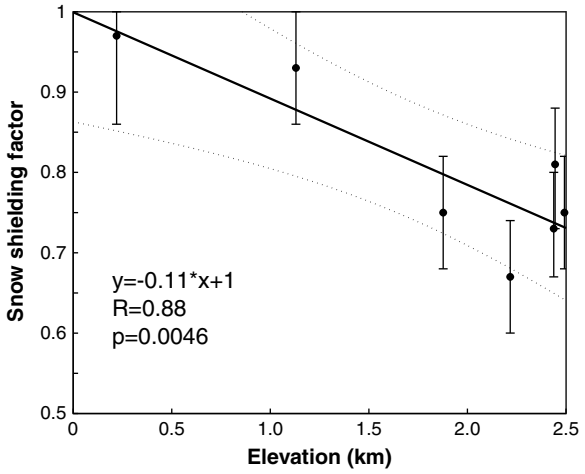

Figure 6. Mean snow shielding factors for seven meteorological stations in the French Alps derived from neutron monitor measurements between 2001 and 2008 [*Delunel*, 2010]. Linear regression yields a significant correlation coefficient of 0.88 ($p < <0.05$). Significance was tested with *t*-statistics.

between 1.5 and 0.1 mm/yr, respectively (see Figure S13). Except for very low erosion rates (<0.2 mm/yr), differences are within typical analytical uncertainties of ^{10}Be analyses, and thus we do not correct ^{10}Be-derived erosion rates for this effect. Incorporation of glacial sediments can further bias catchment-wide erosion rates, especially if the age of glacial sediments is comparable to the erosional timescale and they are eroded by fluvial undercutting [e.g., *Wittmann et al*., 2007]. Although large portions of the study area are covered with glacial sediments, these are predominantly of LGM age, and according to our calculations, surface ^{10}Be concentrations reached quasi steady state considering typical analytical uncertainties [e.g., *Wittmann et al*., 2007].

[24] Snow shielding S^s was estimated from cosmic-ray flux measurements conducted over several years using neutron monitors of nearly horizontal surfaces in the nearby Ecrins-Pelvoux massif [*Delunel*, 2010]. The ratio between the recorded flux in summer (no snow cover) and the mean yearly flux (including winter periods with considerable snow cover) was used as a proxy for snow shielding, assuming that cosmogenic nuclide production scales linearly with the measured neutron fluxes. The data reveal an approximately linear correlation between snow shielding and elevation (Figure 6), which we extrapolated to estimate the corresponding snow shielding for each grid cell in the study area. Hereby, we assume that snowfall in the Isère catchment is spatially invariable and comparable to that in the Ecrins-Pelvoux massif, and that these short-term measurements approximate mean values over the integration time of the ^{10}Be data.

[25] Finally, 1:50000-scale geological maps were used to map the relative quartz contribution of each grid cell; L_i was set to 1 for grid cells containing lithologies that deliver quartz grains within the target grain size fraction (e.g., granite, gneiss, and quartzite) and to 0 for other lithologies (e.g., carbonate, schist). Thus, we calculated production and shielding factors only for grid cells that contain quartz-bearing lithologies (cf. equation 3). Resulting mean shielding factors and production rates are reported in Table 3.

4.3. Cosmogenic ^{10}Be Analytics

[26] All samples have been processed as described by *Delunel et al*. [2010]. Pure quartz was obtained from the nonmagnetic 250–500 μm grain size fraction after repeated etching steps with an H_2SiF_6-HCl mixture following the protocol described by *Brown et al*. [1991]. Atmospheric ^{10}Be attached to grain boundaries was eliminated by three successive treatments with 10% HF dilutions, which in total reduced the sample weight by approximately 30%. After adding approximately 0.3 mL ^{9}Be carrier solution with a concentration of 1000 ppm Be (Scharlau ICP standard batch 03450106), the sample was totally dissolved in a strong HF solution, followed by purification in anion and cation exchange columns. The remaining solution was oxidized to BeO. ^{10}Be/^{9}Be ratios were measured in the French National Accelerator Mass Spectrometry facility Advanced Spaceborne Thermal Emission and Reflection Radiometer (ASTER) in Aix-en-Provence and normalized against National Institute of Standards and Technology (NIST) Standard Reference Materials (SRM) 4325 with the assigned ^{10}Be/^{9}Be ratio of $2.79 \pm 0.03 \times 10^{-11}$.

4.4. Erosion Rates Derived From Detrital Thermochronology

[27] In this study, we used bedrock and detrital AFT thermochronology to estimate erosion rates on the Myr-scale and relative differences in millennial erosion rates, respectively. Both estimates are based on a bedrock AFT-age map of the Isère catchment, interpolated from published bedrock AFT ages [*Lelarge*, 1993; *Seward and Mancktelow*, 1994; *Fügenschuh et al*., 1999; *Fügenschuh and Schmid*, 2003; *Malusà et al*., 2005].

[28] In the simplest case, bedrock thermochronological ages vary only vertically or horizontally, and age maps can be estimated by 2-D interpolation. However, in most regions, bedrock thermochronological ages vary in all spatial directions due to variable uplift rates and/or the perturbation of isotherms caused by pronounced topography and variable rock properties [e.g., *Stüwe et al*., 1994]. In this case, the construction of accurate bedrock-age maps with 2-D interpolation methods requires a high density of age data. To illustrate this issue, we have used a 3-D thermal-kinematic model (Pecube) [*Braun*, 2003; *Braun et al*., 2012] to produce a continuous AFT-age map for a spatially and temporally variable erosion history in the Western Alps (Figures 7a and 7b). Modeling uses steady state topography, a crustal thickness of 35 km, a basal temperature of 600°C, and a heat production of 1 μW/m^3. Time-temperature paths were derived for a spatially and temporally variable exhumation history and corresponding surface AFT ages calculated with the annealing algorithm of *Ketcham et al*. [1999]. Modeled exhumation linearly increases from South to North with a factor of 1.5, and exhumation started at 30 Ma with 0.2 km/Myr in the South (0.3 km/Myr in the North), increasing to 0.6 km/Myr at 5 Ma in the South (0.9 km/Myr in the North).

[29] A 2-D linearly interpolated AFT-age map based on 100 randomly chosen sample points (black dots in Figures 7b–7d) significantly deviates from the modeled AFT-age map (Figure 7c), with a mean age difference of 49%. Comparable results were also found with cubic, nearest neighbor, and the Matlab® "v4" interpolation schemes. Although the regional age pattern (increasing ages to the

Table 3. Cosmogenic-Nuclide Analytical Data, Total Shielding (Topography, Glacier and Snow Cover), Production Rates, and Resulting Catchment-Wide Erosion Rates

Sample Name	Sample Weight (g)	^{10}Be Concentration ($\times 10^3$ at/g)[a]	Total Shielding[b]	Mean Production Rate (at/g yr)[c]		Erosion Rate (m/kyr)[d,e]	
				(1)	(2)	(1)	(2)
CGP 200	3.23	28.72 ± 9.27	0.67	30.12 ± 2.71	21.37 ± 1.92	0.79 ± 0.26	0.56 ± 0.19
CGP 201	23.15	12.17 ± 3.77	0.67	30.20 ± 2.72	21.44 ± 1.93	1.87 ± 0.60	1.33 ± 0.43
CGP 202	19.53	14.49 ± 5.81	0.80	16.01 ± 1.44	14.1 ± 1.27	0.83 ± 0.34	0.73 ± 0.3
CGP 203	9.56	12.54 ± 3.68	0.76	24.69 ± 2.22	19.26 ± 1.73	1.48 ± 0.45	1.16 ± 0.35
CGP 204	10.65	35.31 ± 12.49	0.67	29.20 ± 2.63	18.57 ± 1.67	0.62 ± 0.23	0.39 ± 0.14
CGP 205	7.79	10.39 ± 4.42	0.78	16.73 ± 1.51	13.79 ± 1.24	1.21 ± 0.53	1.00 ± 0.44
CGP 206	20.42	45.13 ± 12.07	0.46	36.42 ± 3.28	16.06 ± 1.45	0.61 ± 0.17	0.27 ± 0.08
CGP 208	16.50	16.74 ± 5.32	0.77	19.11 ± 1.72	16.16 ± 1.45	0.86 ± 0.28	0.73 ± 0.24
CGP 209	11.26	18.63 ± 5.81	0.75	16.91 ± 1.52	14.91 ± 1.34	0.68 ± 0.22	0.60 ± 0.20
CGP 210	14.45	33.72 ± 8.56	0.78	18.29 ± 1.65	15.02 ± 1.35	0.41 ± 0.11	0.33 ± 0.09
CGP 211	19.35	29.88 ± 10.37	0.78	19.35 ± 1.74	15.26 ± 1.37	0.49 ± 0.17	0.38 ± 0.14
RD47	15.72	26.02 ± 2.52	0.76	26.32 ± 2.37	20.21 ± 1.82	0.76 ± 0.17	0.58 ± 0.13
RD48	13.95	31.22 ± 2.60	0.76	26.93 ± 2.42	20.60 ± 1.85	0.65 ± 0.14	0.50 ± 0.11
RD49	11.09	39.98 ± 3.46	0.75	27.84 ± 2.51	21.17 ± 1.91	0.52 ± 0.12	0.40 ± 0.09

[a]Corrected for chemical blank including 1σ analytical and blank errors (associated ^{10}Be/^{9}Be blank ratio was $3.31 \pm 0.76 \times 10^{-15}$). ^{10}Be measurements were calibrated against the National Institute of Standards and Technology (NIST) standard reference material 4325 by using an assigned value of $2.79 \pm 0.03 \times 10^{-11}$ and a ^{10}Be half-life of $1.387 \pm 0.012 \times 10^{6}$ year [*Chmeleff et al*., 2010; *Korschinek et al*., 2010].

[b]Catchment-averaged total shielding factor for quartz-bearing lithologies including (i) topographic- and self-shielding computed according to *Dunne et al*. [1999], (ii) glacier shielding using present-day glacier extent, and (iii) snow shielding, estimated from a linear correlation between elevation and snow shielding derived from cosmic-ray flux measurements [*Delunel*, 2010].

[c]Catchment-averaged surface ^{10}Be production rate based on a modern SLHL ^{10}Be production rate of 4.59 ± 0.40 atoms/g*yr that integrates a spallogenic production rate of 4.49 ± 0.39 atoms/g*yr (cf. section 4.2 for details) [*Balco et al*., 2008 and update to this paper at http://hess.ess.washington.edu/] and scaled for latitude, altitude, and skyline shielding factors. 1σ uncertainty corresponds to ~9% error on scaling factor [*Stone*, 2000; *Balco et al*., 2008 and update to this paper at http://hess.ess.washington.edu/]. (1) Denote raw production rates and (2) are production rates for quartz-bearing lithologies and corrected for total shielding.

[d]Considering field-calibrated measurements provided by *Braucher et al*. [2003], ^{10}Be-derived erosion rates are calculated for neutrons, stopped, and fast muon contributions to the total ^{10}Be surface production rate of 0.9785, 0.015, and 0.0065, respectively, as well as effective attenuation lengths of 150, 1500, and 5300 g cm^{-2} for neutrons, stopped, and fast muons, respectively. A rock density of 2.7 g/cm^3 is used for all calculations. (1) Raw erosion rates and (2) erosion rates corrected for total shielding.

[e]1σ uncertainties include uncertainty on Accelerator Mass Spectrometry (AMS) counting statistics, AMS external error (0.5%), chemical blank measurement, and scaling factor.

South) can be resolved with such a 2-D interpolation, the small-scale accuracy, required for instance to infer spatial differences in catchment erosion rates with detrital thermochronology, is missing. In contrast, the complex age pattern with ages generally increasing both to the South and with elevation is much better retrieved with a linear 3-D interpolation, yielding a mean derivation of 3.2% (11.4% for nearest-neighbor 3-D interpolation) (Figure 7d). The applied 3-D interpolation procedure is based on interpolation functions available in Matlab® and illustrated in Figure 8. Bedrock sample locations (x, y, and z coordinates) with measured AFT ages (Figure 8a) together with a zero AFT-age assumption at −5 km above sea level are used to interpolate a regular 3-D age matrix (Figure 8b) with horizontal and vertical resolution of 1 and 0.1 km, respectively. The zero-age assumption is based on a mean surface temperature of 10°C, an AFT closure temperature of 120°C, and a geothermal gradient of 22°C/km (110°C/22°C/km = 5 km). Note that changing the zero-age depth to −4 or −6 km does not significantly change the resulting age matrix. To obtain the surface age map, the 3-D age matrix is intersected with the DEM; the age of each grid cell of the DEM corresponds to the spatially closest element in the AFT matrix (Figure 8c).

[30] In this study, we extracted Myr-scale erosion rates from such a 3-D interpolated surface AFT-age map assuming a common 1-D steady state thermal structure [*Brandon et al*., 1998], with a model depth of 30 km, a thermal diffusivity of 30 km^2/Myr, a heat production of 8°C/km, a fixed surface temperature of 10°C, a stable (without erosion) surface thermal gradient of 30°C/km, and AFT annealing kinetics from *Ketcham et al*. [1999]. We acknowledge that more evolved methods of estimating Myr-scale erosion rates exist, which take into account potential transient effects [*Rahl et al*., 2007; *Avdeev et al*., 2011] as well as the influence of surface topography on the thermal field [*Braun*, 2002], but for the purposes of our study, these first-order estimates are sufficient.

[31] Furthermore, we used a novel approach to derive millennial-scale estimates of catchment erosion patterns with detrital thermochronology interpreted with respect to an interpolated surface thermochronological age map, comparable but not identical to previous studies [*Brewer et al*., 2003; *Stock et al*., 2006; *Vermeesch*, 2007; *McPhillips and Brandon*, 2010; *Avdeev et al*., 2011; *Tranel et al*., 2011]. Detrital thermochronological age distributions of present-day stream sediments reflect the bedrock thermochronological age pattern within the source area convolved with the potentially spatially variable erosion pattern, as well as differences in bedrock mineral concentrations [e.g., *Resentini and Malusà*, 2012]. Quantifying differences in mineral concentration is very labor-intensive, especially for large catchments like the studied Isère catchment with numerous different outcropping lithologies. We therefore assume here that concentrations of the target mineral (apatite) do not vary significantly in silica-rich crystalline rocks, although a recent study has revealed that such variations may be important [*Tranel et al*., 2011]. Thus, to estimate spatially variable erosion rates, the bedrock-age pattern needs to be quantified.

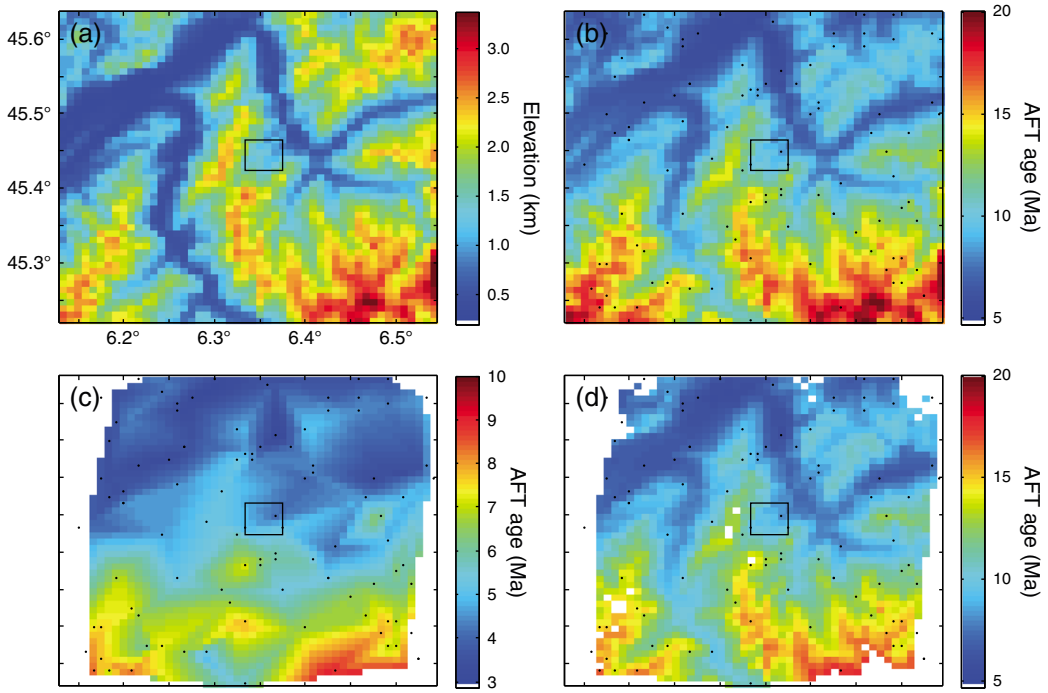

Figure 7. Interpolation of AFT ages in two and three dimensions, exemplified by a synthetic data set. The small rectangle is the extent of the data shown in Figure 8, and black points are 100 randomly selected points. (a) Topography with 1 km resolution. (b) Synthetic AFT ages calculated with Pecube [*Braun*, 2003; *Braun et al*., 2012]. (c) 2-D linear interpolation of AFT ages using the randomly selected points. Mean deviation from the surface AFT-age map in Figure 7b is 49%. (d) 3-D linear interpolation of surface AFT ages using the randomly selected points. Mean deviation from the surface AFT-age map in Figure 7b is 3.2%.

In the simple example shown in Figure 9, thermochronological ages vary linearly with elevation only so that catchment hypsometry reflects the bedrock-age distribution. The latter can then be compared to measured detrital age distributions of stream sediments to decipher the variability of erosion rate with elevation (Figure 9). Although in some regions, this simple age-elevation relationship is applicable [*Brewer et al*., 2003; *Stock et al*., 2006; *Vermeesch*, 2007; *Avdeev et al*., 2011; *Tranel et al*., 2011], applications on larger scales and/or more complex regions require approximation of the 2-D [*McPhillips and Brandon*, 2010] or 3-D (this study) age pattern.

[32] Interpreting the detrital age distribution with respect to the bedrock AFT-age distribution requires taking into

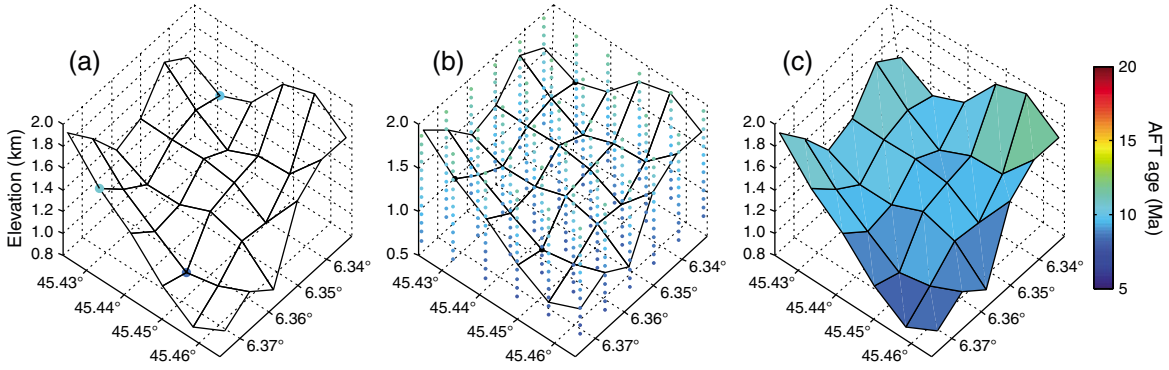

Figure 8. Procedure of 3-D interpolation of bedrock AFT ages to predict surface AFT maps. (a) Subset topography and bedrock AFT ages of the synthetic model in Figure 7. (b) Linearly interpolated AFT ages of 100 randomly chosen sample locations in 3-D (horizontal and vertical resolution of 1 and 0.1 km, respectively). Subset of resulting 3-D AFT matrix is shown in Figure 8b as vertical lines of colored dots (see key to the right), together with sample locations and topography. (c) Resulting surface AFT ages. For each grid cell of the DEM, the AFT age of the spatially closest element in the AFT matrix is used to assign the surface AFT age.

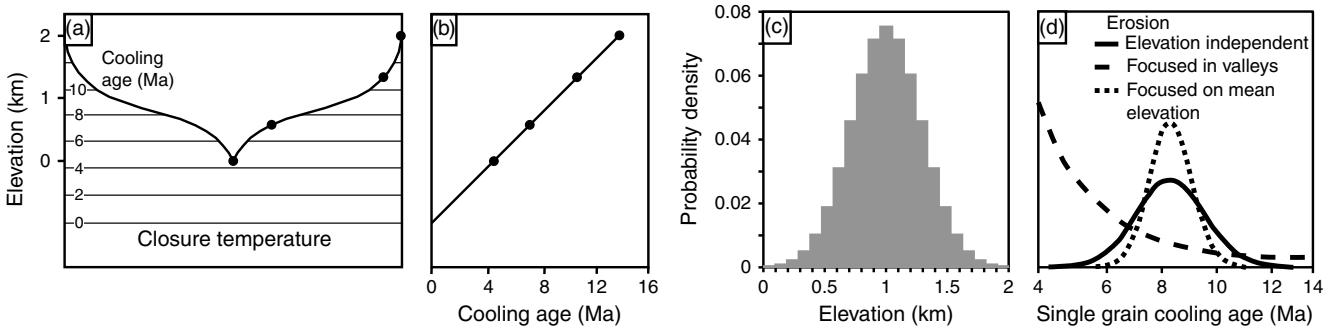

Figure 9. Conceptual model to trace catchment erosion patterns by comparing predicted and measured distributions of detrital cooling ages (modified from *Brewer et al*. [2003]). (a) Hypothetic topographic profile with horizontal cooling age isochrones interpolated from cooling ages of bedrock samples (black dots). (b) Positive linear relationship between bedrock cooling age and sample elevation. (c) Hypsometry of topographic profile shown in Figure 9a. (d) Probability density functions (PDF) of cooling ages derived from a sediment sample assuming different erosion patterns.

account the sample-specific analytical uncertainties (counting statistics). Here we build on the approach of *Vermeesch* [2007] to produce synthetic detrital AFT samples based on relative erosion and bedrock AFT-age maps. Generation of a theoretical detrital age of grain *j* includes the following steps [cf. *Vermeesch*, 2007]:

[33] 1. Randomly select a number of counted induced tracks (N_{ij}) from the measurement database.

[34] 2. Select a bedrock fission-track age (t_j) from the interpolated surface age map, letting the probability of sampling a specific pixel depends on its erosion rate relative to the mean catchment erosion rate. We tested six different temporally constant erosion models: (A) spatially uniform erosion, as expected for a steady state landscape with spatially uniform tectonic and climatic forcing [e.g., *Whipple*, 2001]; (B) erosion decreasing or (C) increasing with elevation, as a result of, e.g., changes in (local) base-level or frost-cracking processes, respectively [e.g., *Delunel et al*., 2010; *van den Berg et al*., 2012]; (D) erosion increasing with slope, as observed in landscapes characterized by hillslopes below the threshold gradient [e.g., *Montgomery and Brandon*, 2002]; (E) erosion increasing with Myr-scale erosion rates from interpolated AFT ages, as expected for steady state landscapes with spatially variable, but temporally constant tectonic and climatic forcing [e.g., *Willett and Brandon*, 2002], and (F) as (E), but increasing relative erosion rates of areas with a Myr-scale erosion rate <0.4 km/Myr by a factor of two. There is no direct theoretical justification for the latter threshold approach; it is rather based on the observed relation between millennial and Myr-scale erosion rates (see section 5). Corresponding relative erosion-rate maps were constructed by linear scaling of parameter maps (e.g., hillslope map) to values between 0 (minimum parameter value) and 1 (maximum parameter value).

[35] 3. Calculate the corresponding number of spontaneous fission tracks (N_{sj}) with the rearranged fission-track age equation [*Hurford and Green*, 1983]:

$$N_{sj} = \frac{N_{ij}}{\lambda_a \rho_d G \zeta} \exp(\lambda_a t_i - 1) \quad (6)$$

in which λ_α is the α-decay constant of ^{238}U, ρ_d is the dosimeter track density, G is the geometry factor, and ζ is a personal calibration factor [e.g., *Hurford and Green*, 1983].

[36] 4. Redetermine N_{ijp} and N_{sjp} from a Poisson distribution with N_{ij} and N_{sj} as mean values, respectively.

[37] Repeating this procedure for the number of counted grains (here 75) results in a synthetic probability-density function (PDF) of predicted single-grain ages for a measured sample. A thousand synthetic PDF have been generated for each erosion model. Statistical methods such as the Kuiper test then allow verifying whether measured and modeled thermochronological ages are drawn from the same distribution. Either they are statistically indistinguishable, which means that the chosen erosion pattern can explain the measured detrital thermochronology data, or they are different and the relative erosion map is dismissed. A unique solution is only obtainable when the analytical uncertainty of the dating method is smaller than minimum difference in bedrock ages, which is generally excluded by the analytical uncertainties of the applied thermochronological method, which are relatively high compared to the variation in bedrock ages.

5. Results

5.1. Geomorphic Analysis

[38] The geomorphic analysis (river long profiles, elevation-hillslope scatterplots, and corresponding histograms) reveals that studied catchments can be roughly subdivided into large catchments (>30 km^2), small "hanging" tributary catchments (<15 km^2), and intermediate catchments. Large catchments are characterized by a stepped profile of the trunk stream; the location of flats and steps are concentrated between the position of the LGM and present-day ELAs (e.g., Figure 4a). In addition, hypsometries reveal a concentration of elevation around 2.0–2.5 km, between the LGM and present-day ELA (Figures 4d and S12), often associated with local minima in mean hillslope plots, similar to observations made immediately south of our study area [*van der Beek and Bourbon*, 2008]. And elsewhere hillslopes generally increase above the local minima and reach their maxima at elevations around or above the present-day ELA (e.g., Figure 4a). Some catchments show a local maximum around the LGM ELA and reach their absolute minimum at minimum elevations.

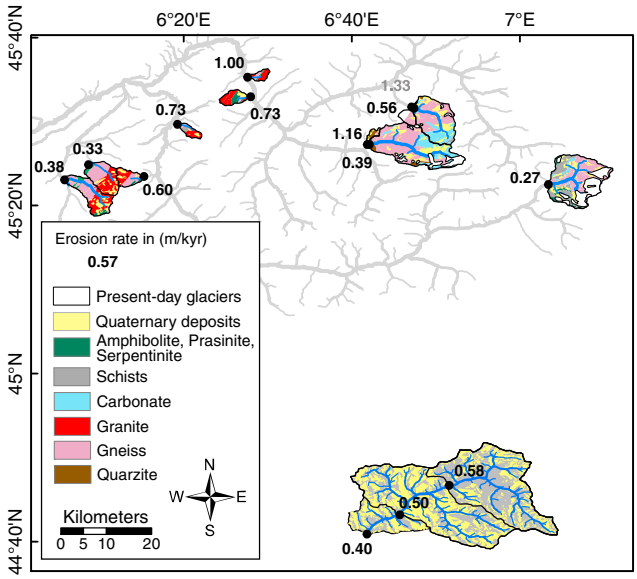

Figure 10. ^{10}Be-derived catchment-wide erosion rates of analyzed catchments. The highest rate (1.33 m/kyr) is measured in a catchment with frequent mudflows (cf. Figure S15). Exposed lithology, Quaternary deposits, and present-day glacier extents within analyzed catchments are from 1:50000 scale BRGM (Bureau de Recherches Géologiques et Minières) geological maps of Albertville (N °726), Bourg-Saint-Maurice (N°727), La Rochette (N°750), Lanselbourg Mont-d'ambin (N°776), Montmelian (N°749), and Tignes (N°752).

Altogether, the morphometry is typical for catchments strongly impacted by focused erosion of large valley glaciers around the ELA. Small catchments (<15 km^2) show more or less convex river long profiles and downstream increasing k_{sn} values (Figures 4e–4g). Hypsometries are not distinct, and mean hillslopes are nearly independent of elevation, whereas the hillslope maximum does not necessarily culminate at maximum elevations. As an example, the catchment of sample CGP203 (4 km^2) exhibits maximum hillslopes (>30°) at its lowest elevations coinciding with the LGM ELA (Figure 4h). We interpret the morphometry of small tributary catchments as a direct result of focused valley incision and widening of the main trunk valleys (Maurienne and Tarentaise Valleys) during repeated glaciations, leading to local base level lowering, development of hanging valleys, and convex river profiles. Medium sized catchments show characteristics of both small and large catchments (e.g., CGP211, see Figure S11).

[39] Mean morphometric measures of studied catchments are comparable to elsewhere in the European Alps [*Wittmann et al.*, 2007; *Delunel et al.*, 2010; *Norton et al.*, 2011]; catchments differ among each other with respect to mean elevation (1.6–2.7 km), hillslope (22–34°), geophysical relief (143–852 m), and normalized steepness index (137–264) (Table 2).

5.2. Millennial Erosion Rates From Cosmogenic Nuclides

[40] Catchment-wide erosion rates, corrected for topographic, glacier, and snow shielding, as well as differences in relative quartz contribution, are between 0.27 m/kyr (CGP206) and 1.33 m/kyr (CGP201), and average over a timescale of ~0.5–2.2 kyr for a mean attenuation length of 60 cm (Table 3, Figure 10). Erosion rates are in the range of rates observed within the Ecrins-Pelvoux massif to the south (0.27–1.07 m/kyr, [*Delunel et al.*, 2010]), as well as more regionally in the Central (0.11–1.58 m/kyr [*Wittmann et al.*, 2007]), Eastern and Southern (0.17–1.4 m/kyr [*Norton et al.*, 2011]) Alps. The lowest erosion rate (0.27 m/kyr, sample CGP206) was measured for a catchment draining the westernmost part of the Gran Paradiso massif, whereas the highest rate (1.33 m/kyr, sample CGP201) comes from a catchment in the adjacent Vanoise region (Figure 10). Erosion rates measured on sediments of the Guil River in the Queyras region are intermediate (~0.5 m/kyr), similar to those of the Belledonne massif. Within the Belledonne massif, erosion rates seem to be higher for catchments draining into the transverse Tarentaise and Maurienne Valleys (~0.75 m/kyr) than for tributary catchments of the axial Isère River (~0.35 m/kyr; Figure 10). The highest variation in erosion rates is observed in the Vanoise region, where analyzed catchments yield rates between 0.39 and 1.33 m/kyr.

[41] Several catchments in the Vanoise region frequently produce mudflows, potentially disturbing the assumption that sampled stream sediments are well mixed [e.g., *Niemi et al.*, 2005; *Yanites et al.*, 2009; *Kober et al.*, 2012]. As a result, catchment-wide erosion rates calculated from such samples may overestimate "real" erosion rates. To assess the potential impact of frequent mudflows, two samples from the Torrent le Ponturin (CGP200 and CGP201) were analyzed (for location, see Figures 2 and 10), one above and one below the confluence with a ~7 km^2 catchment (17% of the total catchment area) that has very recently produced mudflows (see Figure S15). Apparent erosion rates of the upstream and downstream samples are 0.56 and 1.33 m/kyr (Table 3, Figure 10), respectively. Thus, the tributary catchment, even though it is relatively small, obviously delivers large amounts of quartz with low ^{10}Be concentrations, leading to high apparent erosion rates downstream of the confluence. Although our analysis reveals the potential of mudflows to strongly perturb ^{10}Be-derived erosion rates, in the light of our careful sampling strategy, we expect that measured erosion rates of all other samples represent good approximations of mean millennial-scale erosion rates. In the following interpretation and discussion, we will show all samples, but we do not take sample CGP201 into account when establishing correlations with morphometric measures.

5.3. Millennial to Myr-Scale Erosion Rates From Thermochronology

[42] Time integrated Myr-scale erosion rates were estimated from an interpolated bedrock AFT-age map (Figure 11a) and 1-D thermal modeling (for details, see section 4.4). Estimated average Myr-scale erosion rates for the catchments range from 0.12 up to 0.72 km/Myr (Table 2), somewhat lower than ^{10}Be-derived millennial erosion rates (0.27–1.16 m/kyr, Table 3). Myr-scale erosion rates are around or below 0.2 km/Myr for catchments in the internal Alps (east of the Penninic frontal thrust) and around 0.5 km/Myr in the external Alps (west of the Penninic frontal thrust).

[43] The combination of detrital and bedrock thermochronology was applied to track erosion patterns within single catchments

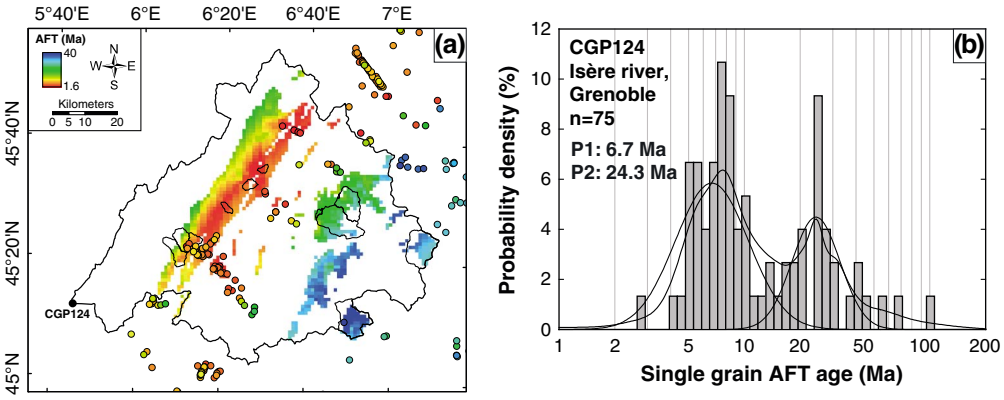

Figure 11. (a) Watershed of sample CGP124 with tributary catchments for which ^{10}Be-based erosion rates have been determined. Bedrock AFT ages of this area [*Lelarge*, 1993; *Seward and Mancktelow*, 1994; *Fügenschuh et al*., 1999; *Fügenschuh and Schmid*, 2003; *Malusà et al*., 2005] are color coded according to their age. Continuous bedrock AFT ages have been estimated from 3-D linear interpolation using Matlab® routines, but only those areas with apatite-bearing lithologies are shown here. (b) AFT-age distribution of sample CGP124 from the Isère River at Grenoble [*Glotzbach et al*., 2011a]. Decomposition of the age distribution into statistically significant age populations using binomial peak fitting [*Stewart and Brandon*, 2004] yielded age peaks of 6.7 Ma (95% CI = 5.8–7.6 Ma) and 24.3 Ma (95% CI = 21.3–27.8 Ma).

[*Brewer et al*., 2003; *Stock et al*., 2006; *Vermeesch*, 2007; *McPhillips and Brandon*, 2010; *Avdeev et al*., 2011; *Tranel et al*., 2011]. The timescale over which this approach is sensitive is on the order of 10^2–10^3 yr, the time needed for comminution and transport of minerals from bedrock to sample sites in streams. In the following, we estimate relative spatial differences in erosion via inversion of a detrital AFT sample from the Isère River (CGP124) [*Glotzbach et al*.,

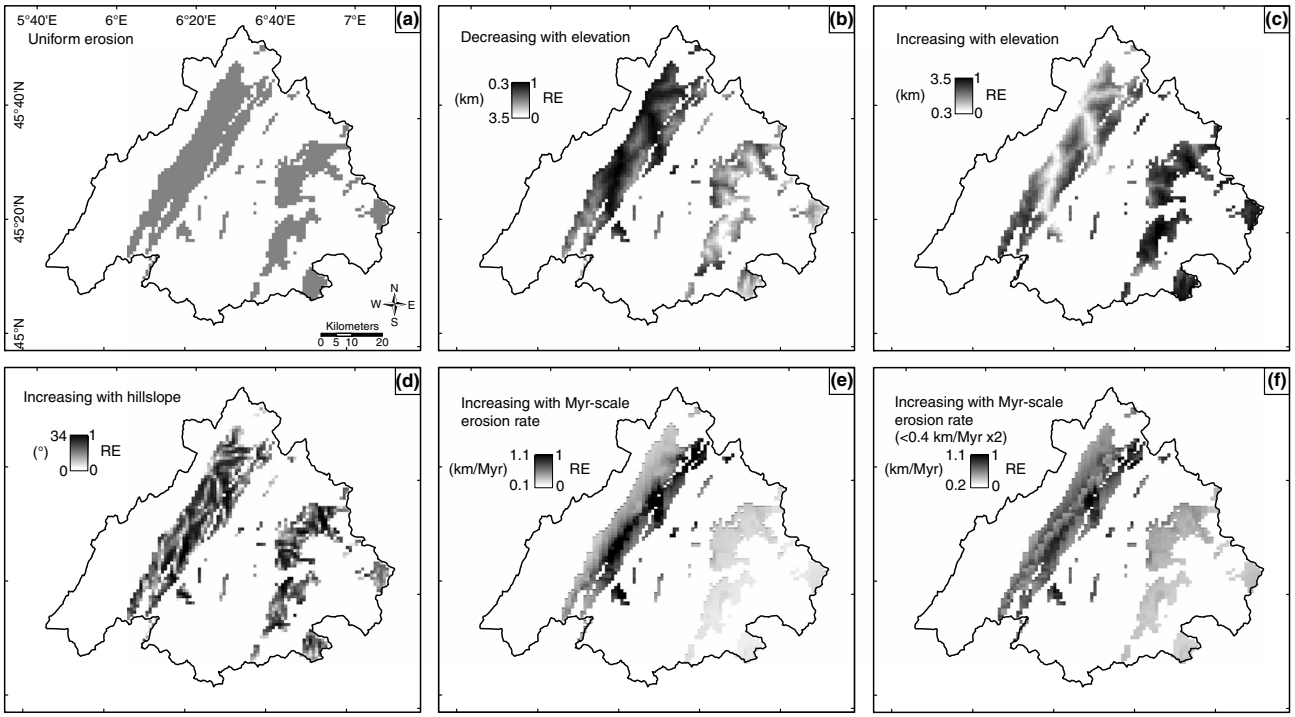

Figure 12. Relative erosion-rate (RE) maps which were used together with the bedrock AFT-age map (Figure 11a) to produce theoretical detrital AFT-age distributions. Grey shading indicates probability of an area to be sampled, with darker shades corresponding to higher probabilities. The probability is either (a) uniform or depends on different parameters, like (b and c) elevation, (d) hillslope, and (e and f) Myr-scale erosion rate, where probabilities have been doubled for pixels with an erosion rate of <0.4 km/Myr in Figure 12f. Parameter ranges have been converted to probability by normalization. Areas that do not contain apatite-bearing rocks have been assigned a probability of 0 (white areas).

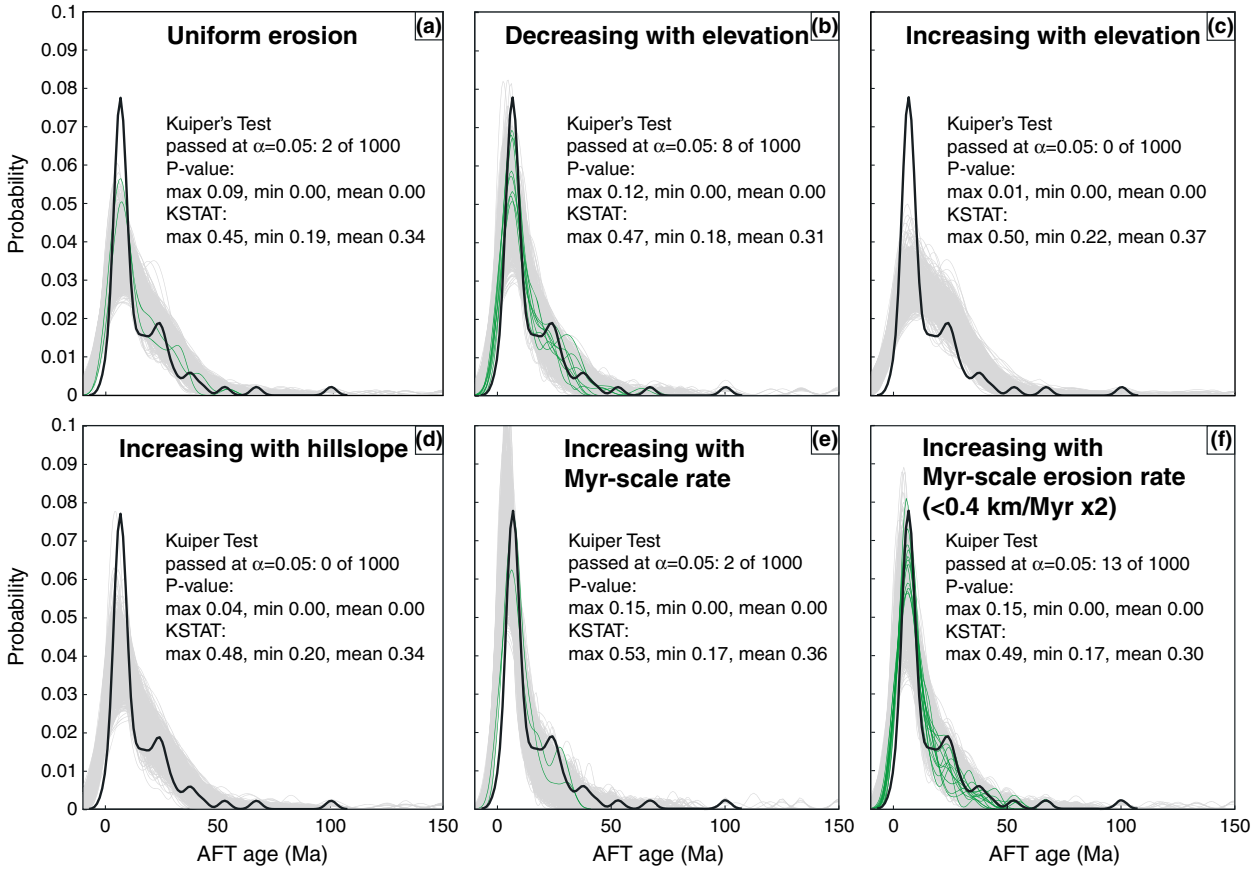

Figure 13. (a–f) Comparison of observed (black) and theoretical (grey or green) AFT-age distributions for sample CGP124 from the Isère River at Grenoble. Theoretical AFT-age distributions are sampled from an interpolated in situ AFT-age map (Figure 11a). Sampling is controlled by probability maps, which reflect the probability of each cell to be sampled (Figure 12). We test uniform and spatially variable erosion, varying with elevation, hillslope, and Myr-scale erosion rate. The Kuiper's test was applied to test whether the two distributions are similar at a significance level of $\alpha = 0.05$. Theoretical AFT-age distributions appear green if they passed the Kuiper's test ($p > 0.05$) and otherwise are grey. KSTAT is Kuiper's statistic, i.e., the maximum difference between the observed and theoretical cumulative PDFs.

2011a]. The corresponding catchment of sample CGP124 encompasses all of the Isère tributary catchments analyzed with cosmogenic ^{10}Be (Figure 11a). Single-grain ages ($n = 75$) of this sample are between 1.3 and 100 Ma (Figure 11b), whereas published bedrock AFT ages within the catchment (64 measurements) vary between 1.6 ± 0.1 and 41 ± 9 Ma (Figure 11a). This apparent discrepancy is due to the high analytical uncertainty of single-grain AFT ages, the oldest detrital single-grain age (100 Ma), for instance, has a 2σ age range between 19 and 522 Ma. AFT ages of bedrock samples have been linearly interpolated in 3-D to obtain a continuous surface AFT-age map (Figure 11a). We exclude areas underlain by lithologies other than sandstone, gneiss, and granite based on a 1:250000 scale geological map. Note that bedrock AFT ages have been reported for some of these excluded areas (Figure 11a); these were, however, sampled from small patches of sandstone within Flysch units or larger calcareous units with overall negligible apatite yield (e.g., Cheval Noir Unit, [*Fügenschuh and Schmid*, 2003]).

[44] Rather than fully invert the detrital AFT data, different erosion models have been used to produce synthetic detrital AFT data that are compared with observed data (see section 4.4 for details). Six different probability (erosion) maps were tested (Figure 12); resulting synthetic age PDFs are shown in comparison with the observed PDF in Figure 13. Kuiper's statistics reveal that some erosion models explain the observed PDF better than others; the "best" models are those where millennial erosion rates are controlled by Myr-scale rates but are doubled for Myr-scale rates < 0.4 km/Myr (13 out of 1000 models pass the test) and models where millennial erosion rates decrease with elevation (8 out of 1000 models pass the test). The rather high failure rate is at least partly due to the low sampling rate; only 75 ages out of 1368 interpolated bedrock ages are sampled according to the erosion rate. Applying the Kuiper test to all possible combinations of two synthetic AFT-age distributions from the same sample reveal that 40% of the data fail the test at a *p*-value of 0.05 (mean *p*-value is 0.2), even though they are sampled from the same distribution. To further increase the fit between observed and synthetic PDF, we suggest that future studies should as far as possible increase the number of analyzed detrital grains.

6. Discussion

[45] In the following discussion, we first identify interactions among our morphometric, cosmogenic, and thermochronologic results, and then investigate the relative contributions of tectonic and climatic forcing to landscape evolution over millennial to Myr timescales. The significance of correlations among environmental, geomorphic, and erosion measures are tested using the *t*-statistic with a significance level of 0.05, and only regressions with significant correlations (p-value <0.05) are reported. In addition, Table 4 reports all cross-correlation coefficients. The analyzed data set is complemented by data from the Ecrins-Pelvoux massif [*Delunel et al*., 2010] and compared to data from the Central and Eastern/Southern Alps [*Wittmann et al*., 2007; *Norton et al*., 2011]. Morphometric indices are mean values for quartz-bearing lithologies only (Table 2), although using values for the entire catchments does not significantly alter observed patterns. We have also tested that observed relations are not biased by the applied snow-shielding correction of ^{10}Be production rates (see Figure S16).

[46] The geomorphic analysis reveals that the present-day landscape bears witness of strong perturbation by repeated major glaciations, but does this climatic perturbation affect millennial and/or Myr-scale erosion rates, and if so, how? We test three contrasting hypotheses (i) the present-day/Holocene climate controls millennial erosion rates, (ii) tectonic forces control the spatial pattern of erosion rates over millennial to Myr timescales, and (iii) Quaternary climate change not only strongly impacted morphometry but has also lead to temporal and spatial variations in erosion rates.

6.1. (Inter)Relations Between Present Climate, Morphometry, and Millennial Erosion Rates

[47] A climate control on erosion has been observed in different mountain ranges over various timescales [e.g., *Finlayson et al*., 2002; *Reiners and Brandon*, 2006; *Moon et al*., 2011]. Mean annual precipitation of analyzed catchments in the Western Alps from measurements between 1971 and 2000 [*Auffray et al*., 2000] correlate positively with geomorphic measures as well as Myr-scale erosion rates (Table 4), however, no significant correlation with millennial erosion rates could be identified (Figure 14a). Recently, *Delunel et al*. [2010] identified another potentially important climate control; they found a significant positive relation ($p = 0.015$) between millennial erosion rates and mean elevation for 12 catchments in the Ecrins-Pelvoux massif. This correlation, in the absence of correlations with any other morphometric measures, was interpreted by *Delunel et al*. [2010] to reflect the control of temperature-dependent (and thus elevation-dependent) frost-cracking efficiency on catchment-wide erosion rates in the massif. The Queyras data follow exactly this trend and both data together yield an even better correlation ($p = 0.009$). Unlike these samples, however, the cosmogenic data from the Isère drainage basin do not show a positive correlation with elevation (Figure 14b). Likewise, detrital thermochronological data are not well predicted by models of increasing erosion with elevation (Figure 13c). Instead, the cosmogenic and thermochronological data can be better explained if erosion scales negatively with elevation (Figures 13b and 14b). In contrast to *Delunel et al's* [2010] data from the Ecrins-Pelvoux massif, the data from *Wittmann et al*. [2007] from the high Central Alps and our new data from the Isère region encompass various tectonic units. We believe that frost cracking in these areas may be as important as in the Ecrins-Pelvoux massif, but its effect could be hidden behind other controls on erosion rates, such as differences in lithology/rock stability and changes in local base level. Based on this, we suggest that the present climate only has a minor impact on millennial erosion rates in complex tectonic settings.

6.2. Does Tectonics Control Erosion and Morphology?

[48] The Myr-scale tectonic setting of the Western Alps is characterized by significant (km-scale) Neogene uplift and resulting erosion of the external crystalline massifs with respect to the internal Alps, as indicated by a strong gradient in surface AFT ages (Figure 11a). No significant linear correlation between mean Myr-scale erosion rates and ^{10}Be-derived millennial erosion rates is observable (Figure 14c). It seems, however, that catchments with relatively high (>0.4 km/Myr) Myr-scale erosion rates, typical for the external crystalline massifs, erode at similar rates on millennial time scales (16 out of 26 samples), but catchments with lower (<0.4 km/Myr) Myr-scale erosion rates, typical for the internal Alps, erode two to three (one sample up to six) times faster on millennial time scales (Figure 14c). These findings are corroborated by the detrital AFT data. Scaling relative erosion linearly with Myr-scale erosion rates yields only a few models that fit the observed detrital AFT distribution (Figures 12e and 13e); most models overpredict the proportion of young ages and, concomitantly, predict too few old ages. Thus, it seems that areas characterized by relatively low Myr-scale erosion rates are at present eroding more rapidly according to the ^{10}Be-derived erosion rates by a factor of >2 (Figure 14c). A corresponding erosion model, in which relative erosion increases with Myr-scale erosion rates, but is also increased by a factor of 2 in areas with Myr-scale erosion rates <0.4 km/Myr (Figure 12f), produces on average the lowest discrepancy between observed and theoretical PDFs (Figure 13f), corroborating the observed trend in ^{10}Be-derived erosion rates. The observed relation becomes even more striking when plotting the spatial distribution of the ratio between ^{10}Be-derived millennial and Myr-scale erosion rates in map view (Figure 15a). Admittedly, mean Myr-scale erosion rates as calculated here average over different time scales (according to their mean AFT age, ranging from 1.6 to 41 Ma) and thus differences in erosion rates possibly incorporate enhanced Quaternary erosion.

[49] Based on these observations, we speculate that the relative impact of Quaternary climate change on millennial erosion rates is stronger in regions with lower Myr-scale erosion rates. According to the stream power model [e.g., *Howard and Kerby*, 1983], steady state channel gradients will increase with rock uplift in rivers with similar erosional efficiency [e.g., *Whipple and Tucker*, 1999]. Therefore, regions uplifting and eroding slowly on the Myr-scale, such as the internal Alps, are characterized (in theory) by shallower river long profiles and less relief compared to rapidly exhuming regions, such as the external crystalline massifs, which may already have had steep rivers and significant relief before the Quaternary [*van der Beek et al*., 2010; *Beucher et al*., 2012; *Sternai et al*., 2012]. In our study area,

Table 4. Cross Correlation Coefficients of Linear Least-Square Fitting Between Morphometric/Environmental and Erosion Measures[a]

Variable	Precipitation	Drainage Area	Elevation	Slope	Steepness Index	Normalized Geophysical Relief	LGM Ice Thickness	Present-Day Ice Extent	Quaternary Deposits	Millennial Erosion	Myr-Scale Erosion
Precipitation	1										
Drainage area	**−0.54**	1									
Elevation	−0.38	0.04	1								
Slope	0.30	−0.15	0.08	1							
Steepness index	**0.60**	**−0.41**	−0.36	0.34	1						
Normalized geophysical relief	0.31	−0.19	−0.09	0.21	**0.57**	1					
LGM ice thickness	0.02	0.07	−0.27	−0.27	0.35	0.13	1				
Present-day ice extent	−0.08	−0.14	**0.77**	0.30	−0.10	−0.06	−0.26	1			
Quaternary deposits	**-0.85**	**0.90**	0.49	**−0.64**	**−0.57**	−0.21	−0.07	−0.12	1		
Millennial erosion	−0.02	**−0.41**	−0.23	−0.23	**0.56**	**0.50**	**0.43**	−0.27	−0.22	1	
Myr-scale erosion	**0.52**	−0.24	−0.38	**0.56**	**0.76**	0.28	**0.39**	0.01	**−0.63**	0.07	1

[a]Bold numbers are statistically significant correlations ($p < 0.05$), tested with *t*-statistics and n − 2 degree of freedom. Note that n differs depending on the number of measures. N is 12 for Quaternary deposits and 25 for short-term denudation, and otherwise 26.

the slowly and rapidly exhuming regions are transversed by the Tarentaise and Maurienne Valleys (e.g., Figure 2), which may have had a major knickzone between these (internal/external) regions before the Quaternary. A shift from uplift-depending river incision to uplift-independent valley incision and widening by glacier erosion [e.g., *Brocklehurst and Whipple*, 2007] may have substantially increased relief in the internal Alps since onset of major glaciations. If this is correct, morphometric parameters (e.g., steepness index) should be in balance with Myr-scale erosion rates in all but the most slowly exhuming regions. In effect, significant correlations with geomorphic measures exist (Table 4), whereas catchments with the lowest estimated Myr-scale erosion rates have relatively high steepness indices that clearly plot off a linear regression line for all data (Figure 15b). Similar multi-methodological studies in other settings are required to confirm these intriguing trends between millennial to Myr-scale erosion rates and geomorphic measures.

[50] Assuming that Myr-scale erosion rates are a proxy for long-term tectonic uplift, it seems that millennial erosion rates are not totally independent of tectonics. Geodetic data reveal a present-day rock-uplift pattern that is spatially less variable than the strong gradient in long-term rock uplift [*Jouanne et al*., 1995; *Brockmann et al*., 2009; *Nocquet et al*., 2011], probably at least partly caused by isostatic compensation due to Holocene erosion and deglaciation [e.g., *Champagnac et al*., 2009]. Thus, the apparent relation between tectonics and millennial erosion rates is likely primarily caused by the positive feedback between climate change and isostatic rock uplift [e.g., *Molnar and England*, 1990].

6.3. What is the Impact of Climate Change on Landscape Evolution and Millennial Erosion Rates?

[51] The present-day landscape of the Western Alps results from the erosional response to periodic Quaternary glaciations, as revealed by geomorphic analyses. Glacial erosion rates can be an order of magnitude higher than fluvial erosion [e.g., *Hallet et al*., 1996] and thus, potentially, markedly alter former fluvial landscapes, although *Koppes and Montgomery* [2009] have recently argued from a reanalysis of data on glacial erosion rates that the potential efficiency of glacial erosion has been overstated. Glacial erosion has been argued to be most efficient around the ELA, where glacier thickness, flux, and sliding rates are maximal [*Humphrey and Raymond*, 1994; *Anderson et al*., 2006].

[52] Major glaciers in the transverse Tarentaise and Maurienne Valleys generated multiple steps in river long profiles and broadened valley bottoms; as a result, tributary valleys hang and show convex river profiles (Figures 3 and 4). Heights of hanging tributary valleys generally increase as the ratio of trunk/tributary ice discharge increases [e.g., *MacGregor et al*., 2000]; thus, glacial impact can be expected to be high for small tributary catchments at or around the position of the ELA. Consequently, geomorphic measures (hillslope, normalized steepness index and normalized geophysical relief) increase with decreasing basin size for all analyzed catchments in the Western Alps, although only normalized steepness indices exhibit a significant relation (Table 4). Interestingly, we also find a significant negative correlation between ^{10}Be-derived erosion rates and basin size in the Isère region (Figure 14d), in which erosion rates appear to increase exponentially with decreasing basin size. Smaller catchments from the Pelvoux-Ecrins massif also follow this trend, but above a threshold of ~50 km^2, erosion rates seem to be independent of basin area. Recently, several studies quantified transient gorge incision into glacially formed hanging valleys [e.g., *Norton et al*., 2010a; *Valla et al*., 2010; *Van den Berg et al*., 2012], demonstrating that incision rates of these features can exceed catchment-wide erosion rates by at least an order of magnitude. Depending on the ratio between the area of the gorge/catchment and erosion rate of the gorge/catchment, catchment-wide erosion rates can be strongly raised, e.g., in the Entlen catchment in central Switzerland by a factor of ~2 [*Van den Berg et al*., 2012]. We speculate that small tributary catchments have a larger fraction of rapidly eroding area as a result of migrating knickpoints (knickzones) developed in incised hanging valleys (convex river segments, e.g., Figure 4), compared to larger upstream trunk valleys. If this is true, geomorphic proxies, such as mean hillslope, relief, and normalized steepness indices, should positively scale with millennial erosion rates. In fact, our data show significant positive correlations of normalized channel steepness indices and geophysical relief with millennial erosion rates (Figures 14e and 14f), whereas ^{10}Be-derived and AFT-derived millennial erosion rates do

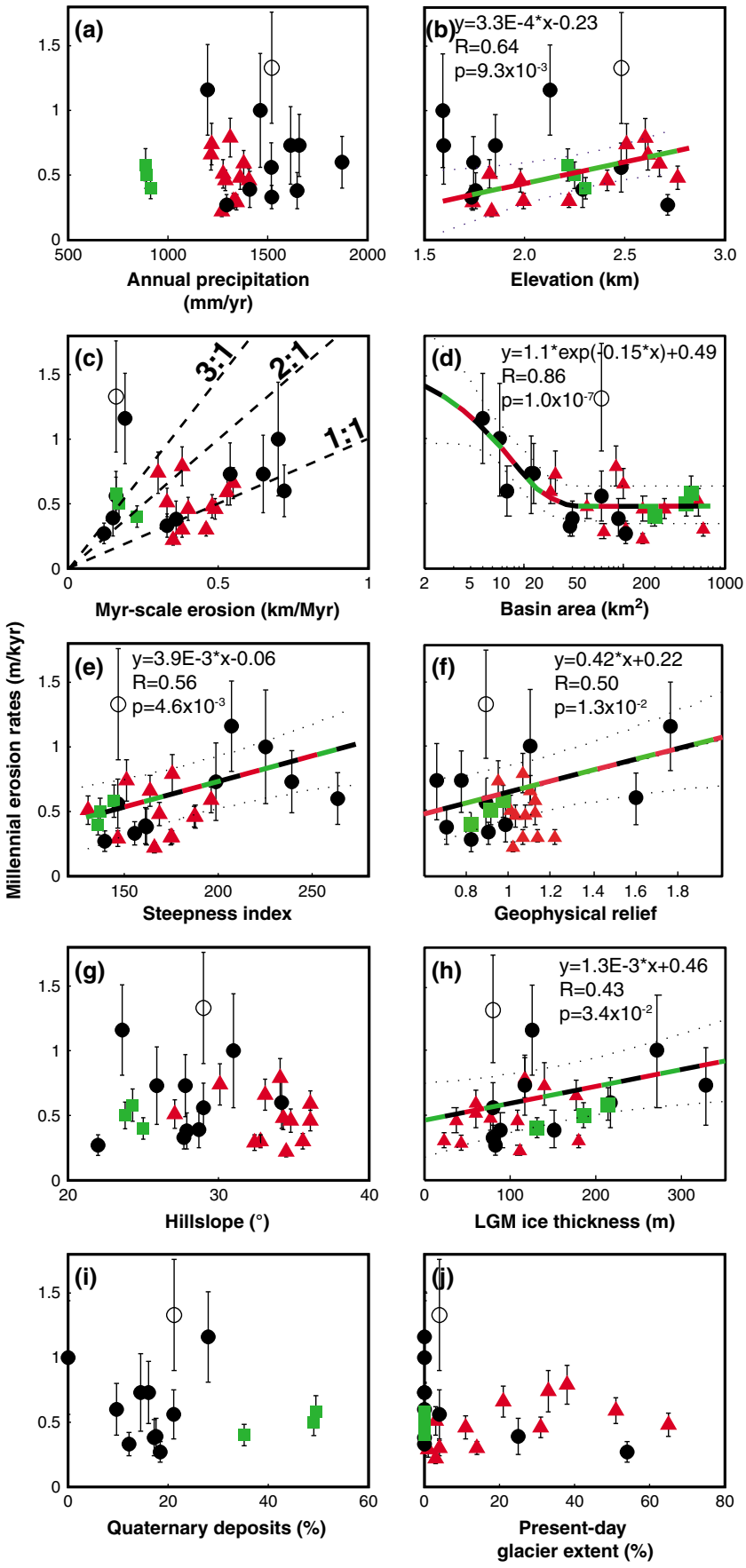
(a)
Annual precipitation (mm/yr)
(b)
y=3.3E-4*x-0.23
R=0.64
p=9.3x10-3
Elevation (km)
(c)
3:1
2:1
1:1
Myr-scale erosion (km/Myr)
(d)
y=1.1*exp(-0.15*x)+0.49
R=0.86
p=1.0x10-7
Basin area (km2)
Millennial erosion rates (m/kyr)
(e)
y=3.9E-3*x-0.06
R=0.56
p=4.6x10-3
Steepness index
(f)
y=0.42*x+0.22
R=0.50
p=1.3x10-2
Geophysical relief
(g)
Hillslope (°)
(h)
y=1.3E-3*x+0.46
R=0.43
p=3.4x10-2
LGM ice thickness (m)
(i)
Quaternary deposits (%)
(j)
Present-day glacier extent (%)

Figure 14

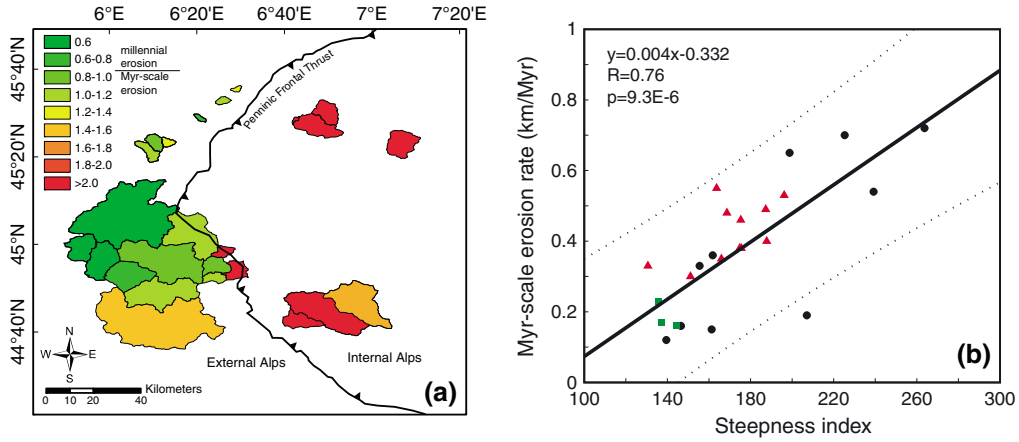

Figure 15. (a) Map showing the ratio of ^{10}Be-derived millennial erosion rates and AFT-derived Myr-scale erosion rates of catchments in the Western Alps. Catchments in the external Alps exhibit ratios around 1, whereas catchments in the internal Alps have ratios around 2 and above. (b) Correlation between mean catchment normalized steepness index and Myr-scale erosion rate. Data from the Isère region are shown as black dots, from the Queyras region as green squares, and from the Ecrins-Pelvoux massif as red triangles.

not scale with hillslope (Figures 12d, 13d, and 14g). The latter finding, however, is not surprising given that mean hillslopes of analyzed catchments (22 to 34°) are close to the failure threshold of hillslopes (~30°) and erosion rates are high. Although transient and local increases in hillslope may have occurred due to glacial erosion (Figure 3), catchment-averaged hillslopes are expected to only depend on rock strength and do not scale with erosion rates [e.g., *Binnie et al.*, 2007; *Ouimet et al.*, 2009; *DiBiase et al.*, 2010; *Palumbo et al.*, 2010]. Similarly, in the high crystalline Alps of the Central, Western, and Eastern Alps, no relation exists between erosion rate and mean hillslope [*Wittmann et al.*, 2007; *Delunel et al.*, 2010; *Norton et al.*, 2011].

[53] A significant positive correlation between millennial erosion rates and mean LGM ice thickness (Figure 14h) corroborates our previous argument. Assuming that erosion rates in small tributary catchments are more likely controlled by the erosional power of the glacier of the trunk valley, the mean LGM ice thickness in tributary catchments may not be an appropriate proxy for millennial erosion rate. Therefore, it is not surprising that the sample from the smallest catchment (CGP203) clearly plots off the apparent linear relationship. Excluding this sample, the significance of the correlation substantially improves from 3.4×10^{-2} to 7.0×10^{-4} (R improves from 0.43 to 0.65).

[54] After the general retreat of glaciers since the LGM, large masses of unconsolidated glacial debris are prone to fluvial mobilization [e.g., *Hinderer*, 2001], especially when deposited on glacially over-steepened landscape features, such as steep valley sides and hanging valleys. Destabilization and consequent landsliding of over-steepened hillslopes together with increased removal of loose deposits from steep hillslopes result in peak erosion rates up to 3 m/kyr during Late Glacial times [*Hinderer*, 2001]. As a result, glacial debris is currently restricted to low-relief areas; for instance, in the Guil River catchments areas mapped as glacial debris (on the 1:50000 scale geological map) exhibit a mean hillslope angle of 23° compared to 26° for areas without mapped glacial debris. Significant negative cross-correlations between the extent of glacial debris and geomorphic measures support this

Figure 14. ^{10}Be-derived catchment-wide erosion rates plotted against mean catchment environmental/morphometric indices of quartz-bearing lithologies only: (a) Annual precipitation rates from measurements between 1971 and 2000 [*Auffray et al.*, 2000], (b) Elevation, (c) Myr-scale erosion rates derived from 1-D steady state thermal modeling of an interpolated surface AFT map (for details, see section 4.4), (d) Basin area, (e) Steepness index normalized with a reference concavity of 0.45, calculated with Stream Profiler (http://www.geomorphtools.org), (f) Geophysical relief normalized by the square root of basin area, (g) Hillslope, calculated as the arc tangent of the steepest gradient of a 3×3 moving window (eight neighbor cells), (h) LGM ice thickness calculated by subtracting the present-day topography from the LGM ice-surface map of *Coutterand* [2010], (i) Surface coverage with Quaternary deposits mapped from 1:50000 scale geological maps, and (j) Surface coverage with present-day glaciers mapped from 1:50000 scale geological maps. Data from the Isère are shown as black dots (reliable data) or as open circle (excluded data, CGP201) and from the Queyras region as green squares. Red triangles represent data from the Ecrins-Pelvoux massif from *Delunel et al.* [2010]. Weighted linear regressions and correlation coefficients were computed with 1σ errors of ^{10}Be-derived erosion rates [e.g., *Williamson*, 1968]. The significance of the correlation coefficient was tested using *t*-statistics with a significance level of 0.05, but only correlations with a p-value <0.05 are shown. Significant correlations were found between catchment-wide erosion rates and (i) mean elevation in the Ecrins-Pelvoux massif and Queyras region, (ii) mean basin area, (iii) mean normalized geophysical relief and steepness index, and (iv) LGM ice thickness for the entire data set.

conclusion (Table 4). The present-day distribution of Quaternary glacial deposits, however, does not show a significant correlation with ^{10}Be-derived erosion rates (Figure 14i). The same applies for the present-day glacier extent of analyzed catchments (Figure 14j).

[55] The geomorphic analysis and observed relations between millennial erosion rates, morphometric measures, and LGM ice thickness suggest that Quaternary glaciations strongly impacted the preglacial topography, leading to transient variations in erosion rates.

6.4. Comparing Millennial to Myr-Scale Erosion Rates in the Alps

[56] ^{10}Be-derived catchment-wide erosion rates in the Western, Central, and Eastern Alps rarely exceed ~1 m/kyr [*Wittmann et al*., 2007; *Delunel et al*., 2010; *Norton et al*., 2010a, 2011], and thus are clearly lower than inferred Late Glacial erosion rates of 1.1–2.9 m/kyr, derived from post-LGM valley and lake fillings and assuming that early Holocene erosion rates are half of modern ones [*Hinderer*, 2001]. Comparing ^{10}Be-derived millennial erosion rates with Myr-scale erosion rates from thermochronology in the Western Alps reveals either comparable rates or significantly higher millennial rates (Figure 14c). In fact, millennial erosion rates in rapidly eroding catchments in the external Western Alps agree with Myr-scale erosion rates, whereas slowly eroding areas (<0.4 km/Myr) in the internal Western Alps are markedly affected by a recent (Quaternary or even post-LGM?) increase in erosion rates (Figures 14c and 15a). In the Central Alps, millennial erosion rates are also about twice as high as the long-term rates inferred from AFT ages [*Wittmann et al*., 2007]. Calculation of mean Myr-scale catchment-wide erosion rates from interpolated bedrock AFT data for analyzed catchments in the Central Alps corroborates these findings and further shows that the relative increase is independent of Myr-scale erosion rates (see Figure S17). Quaternary glaciations appear to have led to an increase in incision rates of major Alpine Valleys (up to 1–1.5 m/kyr) and associated doubling in relief since ~0.9 Ma [*Haeuselmann et al*., 2007; *Glotzbach et al*., 2011b; *Valla et al*., 2011]. Integrated Quaternary erosion rates outside major valleys are not quantified yet, but low-temperature thermochronology suggests that rates are most likely less perturbed from the Myr-scale trend. As an example, zircon and apatite fission track and apatite (U-Th)/He ages from the central Gotthard external crystalline massif in the Central Alps show no evidence for an increase in erosion rate, but suggest erosion with a mean rate of ~0.5 km/Myr since ~14 Ma [*Glotzbach et al*., 2010], although ^{10}Be-derived erosion rates of catchments draining the Gotthard massif to the north and south are 1.58 ± 0.41 m/kyr (Reuss River) and 0.80 ± 0.24 m/kyr (Ticino River), respectively [*Wittmann et al*., 2007]. Overall, the data are consistent with increased Holocene erosion rates compared to Myr-scale erosion rates, which we attribute to be caused by transient disequilibrium introduced in the landscape by glaciations [e.g., *Norton et al*., 2010b].

6.5. Driving Forces of Millennial to Myr-Scale Erosion Rates

[57] There is a clear link between erosion rate and landscape morphology in purely fluvial landscapes, such that tectonically driven rock uplift steepens channels, increases relief, and potentially increases channel incision, which dictates rates of hillslope erosion [e.g., *Howard et al*., 1994; *Whipple*, 2004]. Recent cosmogenic erosion rate studies confirm these relations [e.g., *Binnie et al*., 2007; *Ouimet et al*., 2009; *DiBiase et al*., 2010; *Palumbo et al*., 2010; *Henck et al*., 2011]. However, in glacially affected landscapes, these relations can be obscured or absent [e.g., *Norton et al*., 2010b, 2011]. Large portions of Earth's northern hemisphere have been glaciated during the LGM [e.g., *Ehlers and Gibbard*, 2004a,2004b] and to a smaller extent during Late Glacial glacier advances [e.g., *Ivy-Ochs et al*., 2009]. The Western Alps show characteristic glacial landforms, such as "U-shaped" flat-floored valleys, hanging valleys, cirques, horns, and arêtes [*van der Beek and Bourbon*, 2008]. Geomorphic analyses, in particular the observed significant relation between millennial erosion rates and LGM ice thicknesses, demonstrate a strong impact of glacial erosion on landscape morphometry. Thus, the study area is far from a purely fluvial landscape; nevertheless, the presented data reveal a significant relationship between millennial erosion rates and landscape morphometry (Figures 14e and 14f). Similar to previous studies in fluvially carved landscapes, we find that normalized steepness index and geophysical relief, rather than hillslope, can be reliable geomorphic proxies for erosion rate also in transient postglacial landscapes.

[58] Geomorphic and modeling studies suggest that glaciers generally reduce gradients of main valleys, reducing drainage density and as a result increasing relief [e.g., *Brocklehurst and Whipple*, 2007], while at the same time mean elevation will be reduced [e.g., *Brocklehurst and Whipple*, 2002]. In contrast, tributary channels can be steepened, especially if they are directly connected to glacially overdeepened valleys (such as tributaries in the lower Tarentaise and Maurienne Valleys), assuming that ridgelines stay at constant elevations. Based on these observations, we hypothesize that major glaciations increased channel steepness and relief through base-level lowering in the Western Alps, and as a result led to high transient erosion rates, especially in small tributary catchments. Differences in Myr-scale rock uplift seem to have no control on glacial erosion in the Western Alps, corroborating earlier findings [e.g., *Brocklehurst and Whipple*, 2007; *Foster et al*., 2010]. Although ^{10}Be-derived erosion rates in the Eastern Alps and high Central Alps are clearly increased by Quaternary glaciations, no significant correlation with morphometry could be detected [e.g., *Wittmann et al*., 2007], which may be explained by considerable lithological control on erosion rates [*Norton et al*., 2010b, 2011].

[59] The presented data, especially from the Western Alps, confirm that millennial erosion rates are decoupled from tectonically driven Myr-scale erosion rates. Both ^{10}Be-derived catchment-wide erosion rates and the combination of detrital and bedrock thermochronological data consistently reveal increased millennial erosion rates in areas eroding slowly on the Myr-timescale (<0.4 km/Myr, internal Western Alps), by at least a factor of two. In contrast, the increase in millennial erosion rates in areas that erode rapidly on Myr-timescales, such as the external Western Alps, is relatively minor; however, millennial rates in these catchments still exceed those in the internal Western Alps. Even

though the relative increase seems to be stronger in the internal Western Alps, resolving the impact and temporal variation of erosion rates since Quaternary glaciations remains pending. Recent studies have demonstrated that even when applying state-of-the-art thermochronological methods and numerical modeling, a reliable prediction of such an increase in Myr-scale erosion rates requires that a critical rock column (>1 km) has been removed since initiation of the increase [e.g., *Shuster et al*., 2005; *Glotzbach et al*., 2011b; *Valla et al*., 2012]. Detection thus requires mean Quaternary erosion rates of >1.1 km/Myr (1 km/0.9 Ma), at least five times higher than mean Myr-scale erosion rates, which are between 0.12 and 0.23 km/Myr for analyzed catchments in the internal Western Alps (Table 2).

[60] The nearly balanced millennial erosion rates of the external and internal parts of the Western Alps imply a minor role for neotectonics. Although the external parts of the Western Alps are at present under oblique compression [e.g., *Sue et al*., 1999, 2007] and the internal Alps are characterized by major orogen-parallel and minor orogen-perpendicular extension, millennial erosion rates differ much less than Myr-scale erosion rates (Figure 14c). This similarity in millennial erosion rates, especially in the Ecrins-Pelvoux and Queyras data, suggests that ongoing extensional faulting on the PFT [e.g., *Sue et al*., 2007] only has a minor influence on millennial erosion rates, although it may have been important for the long-term erosion of the external crystalline massifs in the footwall [*Tricart et al*., 2006].

6.6. Erosion Model

[61] Overall, the presented data are consistent with a model in which Myr-scale erosion trends, as recorded by thermochronology, are controlled by tectonics, and glacial preconditioning of the morphology drives millennial ^{10}Be-derived erosion rates. Assuming that the pre-Quaternary landscape of the Western Alps was in steady state [e.g., *Sternai et al*., 2012], we speculate that at that time, the relief of slowly exhuming regions in the internal Western Alps was less pronounced than that of the external Alps, as indicated by observed significant correlations between Myr-scale erosion rates and morphometric measures (Table 4). Indeed, large-scale erosion of the internal Western Alps occurred during Penninic thrusting in Paleogene times, while the external Western Alps were only exhumed since the onset of thrusting along a crustal-scale ramp below the external crystalline massifs in the Neogene [e.g., *Schmid et al*., 1996]. Since initiation of major Quaternary glaciations at ~0.9 Ma, the main valleys began to incise more rapidly, resulting in an approximate doubling in relief [*Haeuselmann et al*., 2007; *Glotzbach et al*., 2011b; *Valla et al*., 2011]. Although the sequence of incision and relief development during repeated Quaternary glaciations remains not well understood, the data may indicate a more or less continuous evolution [e.g., *Haeuselmann et al*., 2007]. In any case, the Western Alps landscape has been strongly impacted, with the effect that despite the gradient in Myr-scale erosion rates, morphometric measures have been adjusted to repeated Quaternary glaciations. We find that, despite the large difference in time scale, Myr-scale erosion rates also correlate positively with geomorphic measures. Slowly exhuming areas, however, do show an offset toward steeper channels and relief, supporting the idea that the internal Western Alps have been impacted relatively more strongly by Quaternary glaciations than the external Western Alps, which may already have had significant relief before the Quaternary [*van der Beek et al*., 2010; *Beucher et al*., 2012]. It seems that the impact is mainly restricted to morphometry, with no sign of markedly offset Myr-scale erosion rates, such as observed in the external Western Alps [e.g., *Glotzbach et al*., 2011b]. The overall result of Quaternary climate change is a leveling of millennial erosion rates of otherwise tectonically controlled differentially uplifting and eroding regions.

7. Conclusions

[62] In this study, we have investigated the driving forces of millennial to Myr-scale erosion in the Isère and Queyras regions in the Western Alps, applying geomorphic analyses, *in situ* produced cosmogenic nuclides (^{10}Be) in stream sediments and a combination of detrital and bedrock thermochronological analysis.

[63] ^{10}Be-derived erosion rates range from ~0.27 to ~1.33 m/kyr, similar to rates measured elsewhere in the Western, Central, and Eastern/Southern Alps. Despite the strong impact of former and present-day glaciers on landscape morphology, our data apparently corroborate previous studies in fluvially dominated landscapes, which show that normalized steepness index and geophysical relief (normalized by basin area), rather than hillslope, are important geomorphic parameters controlling millennial erosion rates. Together with a significant positive correlation of millennial erosion rates with LGM ice thickness, we suggest that transient landscape perturbation due to repeated Quaternary glaciations results in increased millennial erosion rates. Despite the difference in timescale, millennial ^{10}Be-derived erosion rates of areas eroding rapidly on the Myr-scale (>0.4 km/Myr) are comparable to mean Myr-scale erosion rates derived from interpolated bedrock AFT data. Areas that were eroded more slowly (<0.4 km/Myr) on the Myr-scale, in contrast, exhibit a twofold to threefold (and up to sixfold) increase in millennial erosion rates. A similar spatial pattern of millennial erosion rates is also predicted by fitting observed detrital AFT-age distributions. Furthermore, a significant correlation between Myr-scale erosion rate and morphometric measures (in particular steepness index) is observed in the Western Alps. Slowly exhuming areas, however, clearly deviate from this relation, exhibiting "too steep" channels. Based on these findings, we suggest that landscape perturbation due to Quaternary glaciations was independent of rock uplift, and thus the present-day morphometry is less variable than that of the inferred preglacial landscape. As a result, millennial erosion rates are nearly similar in the external and internal Western Alps. Thus, glacial inheritance in landscapes can have a strong control on transient millennial erosion rates of otherwise differentially uplifting and eroding regions controlled by tectonics. The observed consistency between ^{10}Be-derived erosion rates and detrital thermochronology of present-day stream sediments interpreted with respect to bedrock thermochronological age maps strengthens the reliability of the results and also suggests that the latter is a feasible approach to test landscape evolution models.

[64] **Acknowledgments.** This study was funded by Agence Nationale de la Recherche project ANR-08-BLAN-0303-01 "Erosion and Relief Development in the Western Alps" and by the INSU-CNRS through the European Science Foundation (ESF) Eurocores Topo-Europe programme 07-TOPO-EUROPE-FP-023 "Coupled climatic/tectonic forcing of European topography revealed through thermochronometry (Thermo-Europe)". We greatly appreciate the support by INSU-CNRS for AMS measurements at the ASTER facility at Aix-en-Provence. We thank Editor A. Densmore, Associate Editor S. Brocklehurst, and four anonymous reviewers for their helpful and constructive comments and suggestions, which significantly improved the manuscript.

References

Anders, A. M., S. G. Mitchell, and J. H. Tomkin (2010), Cirques, peaks, and precipitation patterns in the Swiss Alps: Connections among climate, glacial erosion, and topography, *Geology*, *38*, 239–242.

Anderson, R. S., P. Molnar, and M. A. Kessler (2006), Features of glacial valley profiles simply explained, *J. Geophys. Res.*, *111*, F01004, doi:10.1029/2005JF000344.

Auffray, A., A. Brisson, A. Tamburini, V. Dziak, V. Maloisel, and S. Martinoni-Lapierre (2000), Climat de la région Rhône-Alpes, *Météo-France Centre-Est*.

Avdeev, B., N. A. Niemi, and M. K. Clark (2011), Doing more with less: Bayesian estimation of erosion models with detrital thermochronometric data, *Earth Planet. Sci. Lett.*, *305*, 385–395.

Balco, G., J. O. Stone, N. A. Lifton, and T. J. Dunai (2008), A complete and easily accessible means of calculating surface exposure ages or erosion rates from 10Be and 26Al measurements, *Quat. Geochronol.*, *3*, 174–195.

Beaumont, C., P. Fullsack, and J. Hamilton (1992), Erosional control of active compressional orogens, in *Thrust Tectonics*, edited by K. R. McClay, pp. 1–18, Chapman and Hall, London.

Bermudez, M. A., P. A. van der Beek, and M. Bernet (2013), Strong tectonic and weak climatic control on exhumation rates in the Venezuelan Andes, *Lithosphere*, *5*, 3–16.

Beucher, R., P. van der Beek, J. Braun, and G. E. Batt (2012), Exhumation and relief development in the Pelvoux and Dora-Maira massifs (Western Alps) assessed by spectral analysis and inversion of thermochronological age transects, *J. Geophys. Res.*, *117*, F03030, doi:10.1029/2011JF002240.

Binnie, S. A., W. M. Phillips, M. A. Summerfield, and L. K. Fifield (2007), Tectonic uplift, threshold hillslopes, and denudation rates in a developing mountain range, *Geology*, *35*, 743–746.

Bonnet, S., and A. Crave (2003), Landscape response to climate change: Insights from experimental modeling and implications for tectonic versus climatic uplift of topography, *Geology*, *31*, 123–126.

Brandon, M. T., M. K. Roden-Tice, and J. I. Garver (1998), Late Cenozoic exhumation of the Cascadia accretionary wedge in the Olympic Mountains, northwest Washington State, *Geol. Soc. Am. Bull.*, *110*, 985–1009.

Braucher, R., E. T. Brown, D. L. Bourlès, and F. Colin (2003), In situ produced ^{10}Be measurements at great depths: Implications for production rates by fast muons, *Earth Planet. Sci. Lett.*, *211*, 251–258.

Braun, J. (2002), Quantifying the effect of recent relief changes on age-elevation relationships, *Earth Planet. Sci. Lett.*, *200*, 331–343.

Braun, J. (2003), Pecube: A new finite-element code to solve the 3D heat transport equation including the effects of a time-varying, finite amplitude surface topography, *Comp. Geosci.*, *29*, 787–794.

Braun, J., P. van der Beek, P. Valla, X. Robert, F. Herman, C. Glotzbach, V. Pedersen, C. Perry, T. Simon-Labric, and C. Prigent (2012), Quantifying rates of landscape evolution and tectonic processes by thermochronology and numerical modeling of crustal heat transport using PECUBE, *Tectonophysics*, *524-525*, 1–28.

Brewer, I. D., D. W. Burbank, and K. V. Hodges (2003), Modelling detrital cooling-age populations: Insights from two Himalayan catchments, *Basin Res.*, *15*, 305–320.

Brocklehurst, S. H., and K. X. Whipple (2002), Glacial erosion and relief production in the Eastern Sierra Nevada, California, *Geomorphology*, *42*, 1–24.

Brocklehurst, S. H., and K. X. Whipple (2007), Response of glacial landscape to spatial variations in rock uplift rate, *J. Geophys. Res.*, *112*, F02035, doi:10.1029/2006JF000667.

Brocklehurst, S. H., K. X. Whipple, and D. Foster (2008), Ice thickness and topographic relief in glaciated landscapes of the western USA, *Geomorphology*, *97*, 35–51.

Brockmann, E., D. Ineichen, U. Marti, S. Schaer, A. Schlatter, and A. Villiger (2009), Determination of tectonic movements in the Swiss Alps using GNSS and levelling, *Internat. Assoc. Geod. Symposium*, Buenos Aires, Argentina.

Brown, E. T., J. M. Edmond, G. M. Raisbeck, F. Yiou, M. D. Kurz, and E. J. Brook (1991), Examination of surface exposure ages of Antarctic moraines using *in situ* produced ^{10}Be and ^{26}Al, *Geochem. Cosmochem. Acta*, *55*, 2269–2283.

Brown, E., R. Stallard, M. Larsen, G. Raisbeck, and F. Yiou (1995), Denudation rates determined from the accumulation of in situ-produced ^{10}Be in the Luquillo experimental forest, Puerto Rico, *Earth Planet. Sci. Lett.*, *129*, 193–202.

Brozović, N., D. Burbank, and A. Meigs (1997), Climatic limits on landscape development in the northwestern Himalaya, *Science*, *276*, 571–574.

Campani, M., F. Herman, and N. Mancktelow (2010), Two- and three-dimensional thermal modeling of the low-angle detachment: Exhumation history of the Simplon Fault Zone, central Alps, *J. Geophys. Res.*, *115*, B10420, doi:10.1029/2009JB007036.

Champagnac, J. D., P. Molnar, R. S. Anderson, C. Sue, and B. Delacou (2007), Quaternary erosion-induced isostatic rebound in the Western Alps, *Geology*, *35*, 195–198.

Champagnac, J.-D., F. Schlunegger, K. Norton, F. von Blanckenburg, L. M. Abbühl, and M. Schwab (2009), Erosion-driven uplift of the modern central Alps, *Tectonophysics*, *474*, 236–249, doi:10.1016/j.tecto.2009.02.024.

Chmeleff, J., F. von Blanckenburg, K. Kossert, and D. Jakob (2010), Determination of the ^{10}Be half-life by multicollector ICP-MS and liquid scintillation counting, *Nucl. Instrum. Meth. Res. B*, *268*, 192–199.

Coutterand, S. (2010), Etude géomorphologique des flux glaciaires dans les Alpes nord-occidentales au Pléistocène récent. PhD thesis, Université de Savoie, Chambéry, France.

Cyr, A. J., D. E. Granger, V. Olivetti, and P. Molin (2010), Quantifying rock uplift rates using channel steepness and cosmogenic nuclide-determined erosion rates: Examples from northern and southern Italy, *Lithosphere*, *2*, 188–198.

Delunel, R. (2010), Evolution géomorphologique du massif des Ecrins-Pelvoux depuis le Dernier Maximum Glaciaire – Apports des nucléides cosmogéniques produits in-situ, PhD thesis, Université Joseph Fourier, Grenoble, France.

Delunel, R., P. A. van der Beek, J. Carcaillet, D. L. Bourlès, and P. G. Valla (2010), Frost-cracking control on catchment denudation rates: Insights from in *situ* produced ^{10}Be concentrations in stream sediments (Ecrins-Pelvoux massif, French Western Alps), *Earth Planet. Sci. Lett.*, *293*, 72–83.

DiBiase, R. A., K. X. Whipple, A. M. Heimsath, and W. B. Ouimet (2010), Landscape form and millennial erosion rates in the San Gabriel Mountains, CA, *Earth Planet. Sci. Lett.*, *289*, 134–144.

DiBiase, R. A., A. M. Heimsath, and K. X. Whipple (2012), Hillslope response to tectonic forcing in threshold landscapes, *Earth Surf. Process. Landforms*, *37*, 855–865.

Dunai, T. (2010), *Cosmogenic Nuclides: Principles, Concepts and Applications in the Earth Surface Sciences*, Cambridge Univ. Press, New York.

Dunne, J., D. Elmore, and P. Muzikar (1999), Scaling factors for the rates of production of cosmogenic nuclides for geometric shielding and attenuation at depth on sloped surfaces, *Geomorphology*, *27*, 3–11.

Egholm, D. L., S. B. Nielsen, V. K. Pedersen, and J.-E. Lesemann (2009), Glacial effects limiting mountain height, *Nature*, *460*, 884–887.

Egholm, D. L., V. K. Pedersen, M. F. Knudsen, and N. K. Larsen (2012), Coupling the flow of ice, water, and sediment in a glacial landscape evolution model, *Geomorphology*, *141-142*, 47–66.

Ehlers, J., and P. L. Gibbard (2004a), Quaternary glaciations – extent and chronology, Part 1: Europe, in *Developments in Quaternary Science, 2a*, 1–475, Elsevier, Amsterdam, Netherlands.

Ehlers, J., and P. L. Gibbard (2004b), Quaternary glaciations – extent and chronology, Part 2: North America, in *Developments in Quaternary Science, 2b*, 1–450, Elsevier, Amsterdam, Netherlands.

Finlayson, D. P., D. R. Montgomery, and B. Hallet (2002), Spatial coincidence of rapid inferred erosion with young metamorphic massifs in the Himalayas, *Geology*, *30*, 219–222.

Flint, J. J. (1974), Stream gradient as a function of order, magnitude, and discharge, *Water Resour. Res.*, *10*(5), 969–973.

Foster, D., S. H. Brocklehurst, and R. L. Gawthorpe (2010), Glacial-topographic interactions in the Teton Range, Wyoming, *J. Geophys. Res.*, *115*, F01007, doi:10.1029/2008JF001135.

Fügenschuh, B., and S. M. Schmid (2003), Late stages of deformation and exhumation of an orogen constrained by fission-track data: A case study in the Western Alps, *Geol. Soc. Am. Bulletin*, *115*, 1425–1440.

Fügenschuh, B., A. Loprieno, S. Ceriani, and S. M. Schmid (1999), Structural analysis of the Subbriançonnais and Valais units in the area of Moûtiers (Savoy, Western Alps): Paeogeographic and tectonic consequences, *Int. J. Earth Sci.*, *88*, 201–218.

Gilbert, G. K. (1877), Report on the Geology of the Henry Mountains, in *U.S. Geograph. Geol. Surv.*, Rocky Mountains Region.

Glotzbach, C., J. Reinecker, Danisik, M. Rahn, W. F., and C. Spiegel (2010), Thermal history of the central Gotthard and Aar massifs, European Alps: Evidence for steady state, long-term exhumation, *J. Geophys. Res.*, *115*, F03017, doi:10.1029/2009JF001304.

Glotzbach, C., M. Bernet, and P. A. van der Beek (2011a), Detrital thermochronology records changing source areas and steady exhumation in the Western European Alps, *Geology*, *39*, 239–242.

Glotzbach, C., P. A. van der Beek, and C. Spiegel (2011b), Episodic exhumation and relief growth in the Mont Blanc massif, Western Alps from numerical modelling of thermochronology data, *Earth Planet. Sci. Lett.*, *304*, 417–430.

Hack, J. T. (1957), Studies of longitudinal stream profiles in Virginia and Maryland, *U.S. Geol. Survey Prof. Paper*, *294-B*, 45–97.

Haeuselmann, P., D. E. Granger, P.-Y. Jeannin, and S.-E. Lauritzen (2007), Abrupt glacial valley incision at 0.8 Ma dated from cave deposits in Switzerland, *Geology*, *35*, 143–146, doi:10.1130/G23094A.

Hallet, B., L. Hunter, and J. Bogen (1996), Rates of erosion and sediment evacuation by glaciers: A review of field data and their implications, *Glob. Planet. Change*, *12*, 213–235.

Henck, A. C., K. W. Huntington, J. O. Stone, D. R. Montgomery, and B. Hallet (2011), Spatial controls on erosion in the Three Rivers Region, southeastern Tibet and southwestern China, *Earth Planet. Sci. Lett.*, *303*, 71–83.

Herman, F., F. Beaud, J.-D. Champagnac, J.-M. Lemieux, and P. Sternai (2011), Glacial hydrology and erosion patterns: A mechanism for carving glacial valleys, *Earth Planet. Sci. Lett.*, *310*, 498–508.

Hinderer, M. (2001), Late Quaternary denudation of the Alps, valley and lake fillings and modern river loads, *Geodin. Acta*, *14*, 231–263.

Howard, A. D., and G. Kerby (1983), Channel changes in badlands, *Geol. Soc. Am. Bull.*, *94*, 739–752.

Howard, A. D., M. A. Seidl, and W. E. Dietrich (1994), Modeling fluvial erosion on regional to continental scales, *J. Geophys. Res.*, *99*, 13,971–13,986.

Humphrey, N. F., and C. F. Raymond (1994), Hydrology, erosion and sediment production in a surging glacier: Variegated Glacier, *J. Glaciol.*, *40*, 539–552.

Hurford, A. J., and P. F. Green (1983), The zeta age calibration of fission-track dating, *Chem. Geol. (Isot. Geosci. Sect.)*, *1*, 285–317.

Hurst, M. D., S. M. Mudd, R. Walcott, M. Attal, and K. Yoo (2012), Using hilltop curvature to derive the spatial distribution of erosion rates, *J. Geophys. Res.*, *117*, F02017, doi:10.1029/2011JF002057.

Ivy-Ochs, S., H. Kerschner, A. Reuther, M. Maisch, R. Sailer, J. Schaefer, P. W. Kubik, H.-A. Synal, and C. Schlüchter (2006), The timing of glacier advances in the northern European Alps based on surface exposure dating with cosmogenic ^{10}Be, ^{26}Al, ^{36}Cl, and ^{21}Ne, in *Application of Cosmogenic Nuclides to the Study of Earth Surface Processes: The Practice and the Potential*, edited by L. L. Siame, D. L. Bourlès, and E. T. Brown, pp. 125–140, Geol. Soc. Am. Spec. Pap., 487.

Ivy-Ochs, S., J. Kerschner, A. Reuther, F. Preusser, K. Heine, M. Maisch, P. W. Kubik, and C. Schlüchter (2008), Chronology of the last glacial cycle in the European Alps, *J. Quat. Sci.*, *23*, 559–573.

Ivy-Ochs, S., H. Kerschner, M. Maisch, M. Christl, P. W. Kubik, and C. Schlüchter (2009), Latest Pleistocene and Holocene glacier variations in the European Alps, *Quat. Sci. Rev.*, *28*, 2137–2149.

Jouanne, F., G. Ménard, and X. Darmendrail (1995), Present-day vertical displacement in the north-western Alps and southern Jura Mountains: Data from leveling comparisons, *Tectonics*, *14*, 606–616.

Kelly, M. A., J.-F. Buoncristiani, and C. Schlüchter (2004), A reconstruction of the last glacial maximum (LGM) ice-surface geometry in the western Swiss Alps and contiguous Alpine regions in Italy and France, *Eclogae Geol. Helv.*, *97*, 57–75.

Ketcham, R. A., R. A. Donelick, and W. D. Carlson (1999), Variability of apatite fission-track annealing kinetics. III. Extrapolation to geological time scales, *Am. Mineral.*, *84*, 1235–1255.

Kirby, E., and K. X. Whipple (2012), Expression of active tectonics in erosional landscapes, *J. Struct. Geol.*, *44*, 54–75.

Kober, F., K. Hippe, B. Salcher, S. Ivy-Ochs, P. W. Kubik, L. Wacker, and N. Hählen (2012), Debris-flow-dependent variation of cosmogenically derived catchment-wide denudation rates, *Geology*, doi:10.1130/G33406.1.

Koons, P. O. (1989), The topographic evolution of collisional mountain belts: A numerical look at the Southern Alps, New Zealand, *Am. J. Sci.*, *289*, 1041–1069.

Koons, P. O. (1990), Two-sided orogen: Collision and erosion from the sandbox to the Southern Alps, New Zealand, *Geology*, *18*, 679–682.

Koppes, M. N., and D. R. Montgomery (2009), The relative efficacy of fluvial and glacial erosion over modern to orogenic timescales, *Nature Geosci.*, *2*, 644–647.

Korschinek, G., et al. (2010), A new value for the half-life of ^{10}Be by heavy-ion elastic recoil detection and liquid scintillation counting, *Nucl. Instrum. Meth. Res. B*, *268*, 187–191.

Lague, D., P. Davy, and A. Crave (2000), Estimating uplift rate and erodibility from the area-slope relationship: Examples from Brittany (France) and numerical modelling, *Phys. Chem. Earth*, *25*, 543–548.

Lal, D. (1991), Cosmic ray labeling of erosion surfaces: In situ nuclide production rates and erosion models, *Earth Planet. Sci. Lett.*, *104*(2-4), 424–439.

Lelarge, L. (1993), Thermochronologie par la méthode des traces de fission d'une marge passive (Dôme de Ponta Grossa, SE Brésil) et au sein d'une chaîne de collision (zone externe de l'arc alpin, France), PhD thesis, Université Joseph Fourier, Grenoble, France.

MacGregor, K. R., R. S. Anderson, S. P. Anderson, and E. D. Waddington (2000), Numerical simulations of glacial-valley longitudinal profile evolution, *Geology*, *28*, 1031–1034.

Malusà, M. G., R. Polino, M. Zattin, G. Bigazzi, S. Martin, and F. Piana (2005), Miocene to Present differential exhumation in the Western Alps: Insights from fission track thermochronology, *Tectonics*, *24*, TC3004, doi:10.1029/2004TC001782.

Matmon, A., P. Bierman, J. Larsen, S. Southworth, M. Pavich, R. Finkel, and M. Caffee (2003), Erosion of an ancient mountain range, the Great Smoky Mountains, North Carolina and Tennessee, *Am. J. Sci.*, *303*, 817–855.

McPhillips, D., and M. T. Brandon (2010), Using tracer thermochronology to measure modern relief change in the Sierra Nevada, California, *Earth Planet. Sci. Lett.*, *296*, 373–383.

Molnar, P., and P. England (1990), Late Cenozoic uplift of mountain ranges and global climate change: Chicken or egg?, *Nature*, *346*, 29–34.

Molnar, P., R. S. Anderson, and S. P. Anderson (2007), Tectonics, fracturing of rock, and erosion, *J. Geophys. Res.*, *112*, F03014, doi:10.1029/2005JF000433.

Montgomery, D. R. (2002), Valley formation by fluvial and glacial erosion, *Geology*, *30*, 1047–1050.

Montgomery, D. R., and M. T. Brandon (2002), Topographic controls on erosion rates in tectonically active mountain ranges, *Earth Planet. Sci. Lett.*, *201*, 481–489.

Moon, S., C. P. Chamberlain, K. Blisniuk, N. Levine, D. H. Rood, and G. E. Hilley (2011), Climatic control of denudation in the deglaciated landscape of the Washington Cascades, *Nature Geosci.*, *4*, 469–473.

Muttoni, G., C. Carcano, E. Garzanti, M. Ghielmi, A. Piccin, R. Pini, S. Rogledi, and D. Sciunnach (2003), Onset of major Pleistocene glaciations in the Alps, *Geology*, *31*, 989–992.

Nicoud, G., G. Royer, J.-C. Corbin, F. Lemeille, and A. Paillet (2002), Creusement et remplissage de la vallée de l'Isère au Quaternaire récent. Apports nouveaux du forage GMB1 (1999) dans la région de Grenoble (France), *Géologie de la France*, *4*, 39–49.

Niemi, N. A., M. Oskin, D. Burbank, A. Heimsath, and E. Gabet (2005), Effects of bedrock landslides on cosmogenically determined erosion rates, *Earth Planet. Sci. Lett.*, *237*, 480–498.

Nocquet, J. M., and E. Calais (2003), Crustal velocity field of Western Europe from permanent GPS array solutions, 1996–2001, *Geophys. J. Int.*, *154*, 72–88.

Nocquet, J.-M., A. Walpersdorf, F. Jouanne, F. Masson, J. Chery, and P. Vernant (2011), Slow deformation in the Western Alps from a decade of continuous GPS measurements, *Geophys. Res. Abstracts*, *13*, EGU2011-11725.

Norton, K. P., and V. Vanacker (2009), Effects of terrain smoothing on topographic shielding correction factors for cosmogenic nuclide-derived estimates of basin-averaged denudation rates, *Earth Surf. Process. Landforms*, *34*, 145–154.

Norton, K. P., F. von Blanckenburg, F. Schlunegger, M. Schwab, and P. W. Kubik (2008), Cosmogenic nuclide-based investigation of spatial erosion and hillslope channel coupling in the transient foreland of the Swiss Alps, *Geomorphology*, *95*, 474–486.

Norton, K. P., F. von Blanckenburg, and P. W. Kubik (2010a), Cosmogenic nuclide-derived rates of diffusive and episodic erosion in the glacially sculpted upper Rhone Valley, Swiss Alps, *Earth Surf. Process. Landforms*, *35*, 651–662.

Norton, K. P., L. M. Abbuhl, and F. Schlunegger (2010b), Glacial conditioning as an erosional driving force in the central Alps, *Geology*, *38*, 655–658.

Norton, K. P., F. von Blanckenburg, R. DiBiase, F. Schlunegger, and P. W. Kubik (2011), Cosmogenic 10Be-derived denudation rates of the Eastern and Southern European Alps, *Int. J. Earth Sci.*, *100*, 1163–1179.

Nye, J. E. (1952), The mechanics of glacier flow, *J. Glaciol.*, *2*, 82–93.

Olivetti, V., A. J. Cyr, P. Molin, C. Faccenna, and D. E. Granger (2012), Uplift history of the Sila Massif, southern Italy, deciphered from cosmogenic ^{10}Be erosion rates and river longitudinal profile analysis, *Tectonics*, *31*, TC3007, doi:10.1029/2011TC003037.

Ouimet, W. B., K. X. Whipple, and D. E. Granger (2009), Beyond threshold hillslopes: Channel adjustment to base-level fall in tectonically active mountain ranges, *Geology*, *37*, 579–582.

Palumbo, L., R. Hetzel, M. Tao, and X. Li (2010), Catchment-wide denudation rates at the margin of the NE Tibet from *in situ*-produced cosmogenic ^{10}Be, *Terra Nova*, *23*, 42–48.

Penck, A. (1905), Glacial features in the surface of the Alps, *J. Geol.*, *13*, 1–19.
Rabatel, A., J.-P. Dedieu, and C. Vincent (2005), Using remote-sensing data to determine equilibrium-line altitudes and mass-balance time series: Validation on three French glaciers, 1994–2002, *J. Glaciol.*, *51*, 539–546.
Rahl, J. M., T. A. Ehlers, and B. A. van der Pluijm (2007), Quantifying transient erosion of orogens with detrital thermochronology from syntectonic basin deposits, *Earth Planet. Sci. Lett.*, *256*, 147–161.
Reiners, P. W., and M. T. Brandon (2006), Using thermochronology to understand orogenic erosion, *Annu. Rev. Earth Planet. Sci.*, *34*, 419–466.
Resentini, A., and M. G. Malusà (2012), Sediment budgets by detrital apatite fission-track dating (Rivers Dora Baltea and Arc, Western Alps), in *Mineralogical and Geochemical Approaches to Provenance*, edited by E. T. Rasbury, S. R. Hamming, and N. R. Riggs, pp. 125–140, Geol. Soc. Am. Spec. Pap., 487.
Riebe, C. S., J. W. Kirchner, D. Granger, and R. Finkel (2000), Erosional equilibrium and disequilibrium in the Sierra Nevada, inferred from cosmogenic 26Al and 10Be in alluvial sediment, *Geology*, *28*, 803–806.
Ring, U., M. T. Brandon, S. D. Willett, and G. S. Lister (1999), Exhumation processes, *Geol. Soc. London Spec. Publ.*, *154*, 1–27.
Schmid, S., B. Fügenschuh, E. Kissling, and R. Schuster (2004), Tectonic map and overall architecture of the Alpine orogen, *Eclogae Geol. Helv.*, *97*, 93–117.
Schmid, S. M., O. A. Pfiffner, N. Froitzheim, G. Schoenborn, and E. Kissling (1996), Geophysical-geological transect and tectonic evolution of the Swiss-Italian Alps, *Tectonics*, *15*, 1036–1064.
Schmidt, K. M., and D. R. Montgomery (1995), Limits to relief, *Science*, *270*, 617–620.
Seward, D., and N. S. Mancktelow (1994), Neogene kinematics of the central and Western Alps: Evidence from fission-track dating, *Geology*, *22*, 803–806.
Shuster, D. L., T. A. Ehlers, M. E. Rusmore, and K. A. Farley (2005), Rapid glacial erosion at 1.8 Ma revealed by $^{4}He/^{3}He$ thermochronometry, *Science*, *310*, 1668–1670.
Shuster, D. L., K. M. Cuffey, J. W. Sanders, and G. Balco (2011), Thermochronometry reveals headward propagation of erosion in an Alpine landscape, *Science*, *332*, 84–88.
Small, E. E., and R. S. Anderson (1998), Pleistocene relief production in Laramide mountain ranges, western United States, *Geology*, *26*, 123–126.
Steer, P., R. S. Huismans, P. G. Valla, S. Gac, and F. Herman (2012), Bimodal Plio-Quaternary glacial erosion of fjords and low-relief surfaces in Scandinavia, *Nature Geosci.*, doi:10.1038/NGEO1549.
Sternai, P., F. Herman, M. R. Fox, and S. Castellfort (2011), Hypsometric analysis to identify spatially variable glacial erosion, *J. Geophys. Res.*, *116*, F03001, doi:10.1029/2010JF001823.
Sternai, P., F. Herman, J.-D. Champagnac, M. Fox, B. Salcher, and S. D. Willett (2012), Pre-glacial topography of the European Alps, *Geology*, *40*, 1067–1070.
Stewart, R. J., and M. T. Brandon (2004), Detrital-zircon fission-track ages for the "Hoh Formation": Implications for late Cenozoic evolution of the Cascadia subduction wedge, *Geol. Soc. Am. Bull.*, *116*, 60–75, doi:10.1130/B22101.1.
Stock, J. D., T. A. Ehlers, and K. A. Farley (2006), Where does sediment come from? Quantifying catchment erosion with detrital apatite (U-Th)/He thermochronometry, *Geology*, *34*, 725–728.
Stone, J. (2000), Air pressure and cosmogenic isotope production, *J. Geophys. Res.*, *105*, 23,753–23,759.
Stüwe, K., L. White, and R. Brown (1994), The influence of eroding topography on steady-state isotherms. Application to fission track analysis, *Earth Planet. Sci. Lett.*, *124*, 63–74.
Sue, C., F. Thouvenot, J. Fréchet, and P. Tricart (1999), Widespread extension in the core of the Western Alps revealed by earthquake analysis, *J. Geophys. Res.*, *104*, 25,611–25,622.
Sue, C., B. Delacou, J.-D. Champagnac, C. Allanic, P. Tricart, and M. Burkhard (2007), Extensional neotectonics around the bend of the Western/Central Alps: An overview, *Int. J. Earth Sci.*, *96*, 1101–1129.
Summerfield, M. A., and N. J. Hulton (1994), Natural controls of fluvial denudation rates in major world drainage basins, *J. Geophys. Res.*, *99*, 13,871–13,883.
Tranel, L. M., J. A. Spotila, M. J. Kowalewski, and C. M. Waller (2011), Spatial variation of erosion in a small, glaciated basin in the Teton Range, Wyoming, based on detrital apatite (U-Th)/He thermochronology, *Basin Res.*, *23*, 571–590, doi:10.1111/j.1365-2117.2011.00502.x.
Tricart, P., P. A. van der Beek, S. Schwartz, and E. Labrin (2006), Diachronous late-stage exhumation across the western Alpine arc: Constraints from apatite fission-track thermochronology between the Pelvoux and Dora-Maira Massifs, *J. Geol. Soc. London*, *163*, 1–12.
U. S. Geological Survey (USGS) (2006), Shuttle Radar Topography Mission, 1 Arc Second scene, Unfilled Finished-A, Global Land Cover Facility, University of Maryland, College Park, Maryland, February 2000.
Valla, P. G., P. A. van der Beek, and J. Carcaillet (2010), Dating bedrock gorge incision in the French Western Alps (Ecrins-Pelvoux massif) using cosmogenic ^{10}Be, *Terra Nova*, *22*, 18–25.
Valla, P. G., D. L. Shuster, and P. A. van der Beek (2011), Significant increase in relief of the European Alps during mid-Pleistocene glaciations, *Nature Geosci.*, *4*, 688–692.
Valla, P. G., P. A. van der Beek, D. L. Shuster, J. Braun, F. Herman, L. Tassan-Got, and C. Gautheron (2012), Late Neogene exhumation and relief development of the Aar and Aiguilles Rouges massifs (Swiss Alps) from low-temperature thermochronology modeling and $^{4}He/^{3}He$ thermochronometry, *J. Geophys. Res.*, *116*, F01004, doi:10.1029/2011JF002043.
van der Beek, P. A., and P. Bourbon (2008), A quantification of the glacial imprint on relief development in the French Western Alps, *Geomorphology*, *97*, 52–72.
van der Beek, P. A., P. G. Valla, F. Herman, J. Braun, C. Persano, K. J. Dobson, F. M. Stuart, and E. Labrin (2010), Inversion of thermochronological age-elevation profiles to extract independent estimates of denudation and relief history – II: Application to the French Western Alps, *Earth Planet. Sci. Lett.*, *296*, 9–22.
van den Berg, F., F. Schlunegger, N. Akçar, and P. Kubik (2012), ^{10}Be-derived assessment of accelerated erosion in a glacially conditioned inner gorge, Entlebuch, Central Alps of Switzerland, *Earth Surf. Process. Landforms*, *37*, doi:10.1002/esp.3237.
Vermeesch, P. (2007), Quantitative geomorphology of the White Mountains (California) using detrital apatite fission track thermochronology, *J. Geophys. Res.*, *112*, F03004, doi:10.1029/2006JF000671.
Vernon, A. J., P. A. van der Beek, H. D. Sinclair, and M. K. Rahn (2008), Increase in late Neogene denudation of the European Alps confirmed by analysis of a fission-track thermochronology database, *Earth Planet. Sci. Lett.*, *270*, 316–329.
Vincent, C. (2002), Influence of climate change over the 20th century on four French glacier mass balances, *J. Geophys. Res.*, *107*(D19), 4375, doi:10.1029/2001JD000832.
von Blanckenburg, F. (2005), The control mechanisms of erosion and weathering at basin scale from cosmogenic nuclides in river sediment, *Earth Planet. Sci. Lett.*, *237*, 462–479.
Whipple, K. X. (2001), Fluvial landscape response time: How plausible is steady-state denudation?, *Am. J. Sci.*, *301*, 313–325.
Whipple, K. X. (2004), Bedrock rivers and the geomorphology of active orogens, *Annu. Rev. Earth Planet. Sci.*, *32*, 151–185.
Whipple, K. X., and B. J. Meade (2004), Controls on the strength of coupling among climate, erosion, and deformation in two-sided, frictional orogenic wedges at steady state, *J. Geophys. Res.*, *109*, F01011, doi:10.1029/2003JF000019.
Whipple, K. X., and G. E. Tucker (1999), Dynamics of the stream-power river incision model: Implications for height limits of mountain ranges, landscape response timescales, and research needs, *J. Geophys. Res.*, *104*, 17,661–17,674.
Whipple, K. X., E. Kirby, and S. H. Brocklehurst (1999), Geomorphic limits to climate-induced increases in topographic relief, *Nature*, *401*, 39–43.
Whittaker, A. C., and S. J. Boulton (2012), Tectonic and climatic controls on knickpoint retreat rates and landscape response times, *J. Geophys. Res.*, *117*, F02024, doi:10.1029/2011JF002157.
Willett, S. D. (1999), Orogeny and orography: The effects of erosion on the structure of mountain belts, *J. Geophys. Res.*, *104*, 28,957–28,981.
Willett, S. D., and M. T. Brandon (2002), On steady states in mountain belts, *Geology*, *30*, 175–178.
Willett, S. D., and M. T. Brandon (2013), Some analytical methods for converting thermochronometric age to erosion rate, *Geochem. Geophys. Geosyst.*, *14*, doi:10.1029/2012GC004279.
Williamson, J.-H. (1968), Least-squares fitting of a straight line, *Can. J. Physics*, *46*, 1845–1847.
Wittmann, H., F. von Blanckenburg, T. Kruesmann, K. P. Norton, and P. W. Kubik (2007), Relation between rock uplift and denudation from cosmogenic nuclides in river sediment in the Central Alps of Switzerland, *J. Geophys. Res.*, *112*, F04010, doi:10.1029/2006JF000729.
Wobus, C. W., K. X. Whipple, E. Kirby, N. P. Snyder, J. Johnson, K. Spyropolou, B. Crosby, and D. Sheehan (2006), Tectonics from topography: Procedures, promise and pitfalls, in *Tectonics, Climate and Landscape Evolution, in Tectonics*, *climate*, *and landscape evolution*, edited by S. D. Willett et al., pp. 55–74, Geol. Soc. Am. Spec. Pap., 398.
Yanites, B. J., G. E. Tucker, and R. S. Anderson (2009), Numerical and analytical models of cosmogenic radionuclide dynamics in landslide-dominated drainage basins, *J. Geophys. Res.*, *114*, F01007, doi:10.1029/2008JF001088.
Zeitler, P. K., et al. (2001), Crustal Reworking at Nanga Parbat, Pakistan: Metamorphic consequences of thermal-mechanical coupling facilitated by erosion, *Tectonics*, *20*, 712–728.